AD-A192 303 IMPROVED POTENTIAL FLOW COMPUTATIONAL METHODS WITH EULER CORRECTIONS FOR (U) MCDONNELL DOUGLAS CORP LONG BEACH CA L T CHEN ET AL 30 SEP 87 MDC-K0445 1/1

UNCLASSIFIED DTRC-AD-CR-01-87 N00167-85-C-0134 F/G 1/1 NL

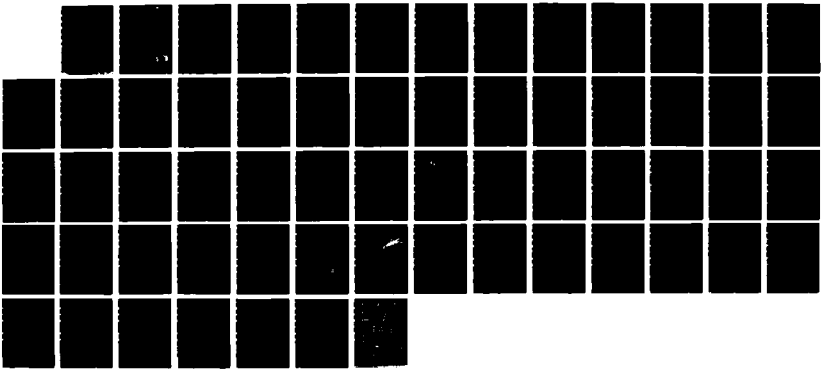

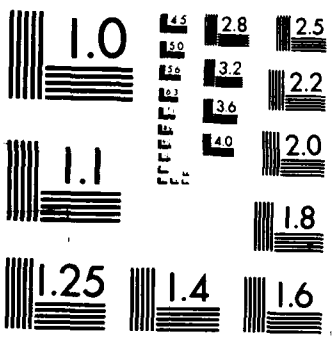
1.0
1.1
1.25
1.4
1.6
1.8
2.0
2.2
2.5
2.8
3.2
3.6
4.0
4.5
5.0
5.6
6.3

Report No. MDC K0445

IMPROVED POTENTIAL FLOW COMPUTATIONAL METHODS WITH EULER CORRECTIONS FOR AIRFOIL AND WING/BODY DESIGN

L. T. Chen and T. Q. Dang
Aerodynamics Research and Technology
Douglas Aircraft Company
McDonnell Douglas Corporation
3855 Lakewood Boulevard
Long Beach, CA 90846

30 September 1987

Final Report for Period 15 September 1985
through 15 September 1987

Approved for public release;
distribution unlimited.

Prepared for
NAVAL AIR SYSTEMS COMMAND
Washington, DC 20361

DAVID TAYLOR RESEARCH CENTER
Bethesda, MD 20084-5000

UNCLASSIFIED
SECURITY CLASSIFICATION OF THIS PAGE

ADA192303

REPORT DOCUMENTATION PAGE

1a REPORT SECURITY CLASSIFICATION UNCLASSIFIED	1b RESTRICTIVE MARKINGS
2a SECURITY CLASSIFICATION AUTHORITY	3 DISTRIBUTION/AVAILABILITY OF REPORT Approved for public release; distribution is unlimited.
2b DECLASSIFICATION/DOWNGRADING SCHEDULE	
4 PERFORMING ORGANIZATION REPORT NUMBER(S) Report MDC K0445	5 MONITORING ORGANIZATION REPORT NUMBER(S) DTRC-AD-CR-01-87
6a NAME OF PERFORMING ORGANIZATION Douglas Aircraft Company McDonnell Douglas Corporation 6b OFFICE SYMBOL (If applicable)	7a NAME OF MONITORING ORGANIZATION David Taylor Research Center
6c ADDRESS (City, State, and ZIP Code) 3855 Lakewood Boulevard Long Beach, CA 90846	7b ADDRESS (City, State, and ZIP Code) Bethesda, MD 20084-5000
8a NAME OF FUNDING/SPONSORING ORGANIZATION Naval Air Systems Command 8b OFFICE SYMBOL (If applicable) Code 931M	9 PROCUREMENT INSTRUMENT IDENTIFICATION NUMBER Contract N00167-85-C-0134
8c ADDRESS (City, State, and ZIP Code) Washington, DC 20361	10 SOURCE OF FUNDING NUMBERS PROGRAM ELEMENT NO: 61153N; PROJECT NO: W2303; TASK NO: —; WORK UNIT ACCESSION NO:

11 TITLE (Include Security Classification)
IMPROVED POTENTIAL FLOW COMPUTATIONAL METHODS WITH EULER CORRECTIONS FOR AIRFOIL AND WING/BODY DESIGN

12 PERSONAL AUTHOR(S)
Chen, L.T. and Dang, T.Q.

13a TYPE OF REPORT	13b TIME COVERED	14 DATE OF REPORT (Year, Month, Day)	15 PAGE COUNT
Final	FROM 8509 TO 8709	1987 September	

16 SUPPLEMENTARY NOTATION

17 COSATI CODES			18 SUBJECT TERMS (Continue on reverse if necessary and identify by block number)
FIELD	GROUP	SUB-GROUP	Clebsch Transformation; Three-Dimensional CFD; Computational Fluid Dynamics; Two-Dimensional CFD; Euler Correction
01	01		
12	01		

19 ABSTRACT (Continue on reverse if necessary and identify by block number)

The development of two- and three-dimensional Euler correction methods based on the Clebsch transformation is described. In these methods, the velocity field is decomposed into irrotational and rotational parts. A multi-grid full-potential method based on both the finite-difference and finite-volume formulations is modified to solve for the irrotational part, while the momentum equation is applied to solve for the rotational part. Two approaches are developed to solve for the rotational field. The approximate Euler-Clebsch approach assumes the entropy is convected along mesh lines, while the exact Euler-Clebsch approach solves the convection of entropy numerically along streamlines. The two approaches agree well in the airfoil application. Only the approximate Euler-Clebsch approach is employed in the three-dimensional calculations. A study of finite-difference and finite-volume formulations of the full-potential equation is

(Continued)

20 DISTRIBUTION/AVAILABILITY OF ABSTRACT	21 ABSTRACT SECURITY CLASSIFICATION
☐ UNCLASSIFIED/UNLIMITED ☒ SAME AS RPT ☐ DTIC USERS	UNCLASSIFIED
22a NAME OF RESPONSIBLE INDIVIDUAL Gregory S. Huson	22b TELEPHONE (Include Area Code) (301) 227-1397
	22c OFFICE SYMBOL Code 1660

DD FORM 1473, 84 MAR — 83 APR edition may be used until exhausted. All other editions are obsolete.

SECURITY CLASSIFICATION OF THIS PAGE
UNCLASSIFIED

(Block 19 continued)

also included. Solutions are presented for various airfoils, wings and an F-14 wing/body and are compared with results of the full-potential and the time-marching Euler methods.

TABLE OF CONTENTS

LIST OF FIGURES

LIST OF TABLES

NOMENCLATURE

a	speed of sound
a_o	stagnation speed of sound
$c_1, c_2 \ldots c_9$	coordinate transformation coefficients defined in Eqs. (4) - (12) and also Eqs. (33) - (37)
D	determinant of Jacobian transformation matrix defined in Eqs. (28) and (42)
$\hat{e}_x, \hat{e}_y, \hat{e}_z$	unit vectors in x,y and z directions
$h_1, h_2 \ldots h_9$	coefficients defined in Eqs. (16) - (24)
H	artificial viscosities at supersonic points defined in Eqs. (50), (53) and (55)
H_s	artificial viscosities at shock points defined in Eqs. (52) and (54)
$H(\xi)$	step function of ξ
M	local Mach number
M_{shock}	Mach number just upstream of the shock
M_∞	freestream Mach number
$\hat{n}$	unit normal to the shock surface
p	local flow pressure
p_m	partially conservative parameter defined in Eqs. (52) and (54)
p_t	total pressure
P_x, P_y, P_z	second-order transformation derivatives defined in Eqs. (25) - (27) and (43) - (44)
q	magnitude of velocity
s	entropy
S	coordinate in streamwise direction
u_∞	freestream velocity
u, v, w	velocity components in x,y, and z directions defined in Eqs. (29) - (31) and (40) - (41)
U, V, W	velocity components defined in Eqs. (12) - (15) and (38) - (39)
$\underline{v}$	velocity vector

v_w	mean wake velocity
x,y,z	coordinates in physical space
X,Y,Z	coordinates in computational space
α	angle of attack
Φ	total velocity potential function
μ	switch function defined in Eq. (51)
ρ	local flow density
ρ_t	total density
τ	material coordinate defined in Eq. (65)
γ	ratio of specific heats
Γ	circulation distribution of the wing
$\underset{\sim}{\Omega}$	vorticity vector
ξ	function defining the location of trailing vortex sheet
$\delta(\xi)$	Dirac data function

ABSTRACT

The development of two- and three-dimensional Euler correction methods based on the Clebsch transformation is described. In these methods, the velocity field is decomposed into irrotational and rotational parts. A multigrid full-potential method based on both the finite-difference and finite-volume formulations is modified to solve for the irrotational part, while the momentum equation is applied to solve for the rotational part. Two approaches are developed to solve for the rotational field. The approximate Euler-Clebsch approach assumes the entropy is convected along mesh lines, while the exact Euler-Clebsch approach solves for the convection of entropy along streamlines. The two approaches agree well in the airfoil application. Only the approximate Euler-Clebsch approach is employed in the three-dimensional calculations. A study of finite-difference and finite-volume formulations of the full-potential equation is also included. Euler-correction solutions are presented for various airfoils, wings and an F-14 wing/body and are compared with results of the full-potential and the time-marching Euler methods.

1.0 INTRODUCTION

Inviscid flow generally can be described by the Euler equations. However, the use of the Euler equations requires the flow density, velocity and energy to be solved as unknown functions. Transonic flows with relatively weak shocks can be assumed to be isentropic and approximated by potential flow methods where the potential function is solved as the only unknown function, thus requiring much less computation than the Euler methods. In the past fifteen years transonic computational methods for solving for the potential flowfields have been well developed, extensively validated, and widely accepted as a routine tool for aerodynamic design. Methods for solving the Euler equations were introduced at a later stage, and significant progress has been achieved in this area recently. However, because of the much greater memory and computational time requirements of the Euler methods, and also their less complete validation [1-2], the full-potential methods are still preferred in the routine transonic aerodynamic design.

Although the existing full-potential methods are limited to problems dealing with relatively weak shocks, they are ideal for simulating transonic flowfields

at cruise conditions. The solution accuracy of the full-potential method deteriorates as the flow condition approaches stall where the shocks become much stronger. To further improve existing full-potential methods, and extend their applications to stronger shock cases, the effects of the total pressure loss across shocks and the vorticities generated downstream of the shocks on the solutions have to be studied carefully. This can be accomplished by the so-called Euler correction methods that are derived from the basic full-potential methods by add- ing additional terms to model the nonisentropic effects.

This report describes several improvements of the existing transonic full-potential method, including the development of an Euler correction method using the Clebsch transformation. Both finite-difference and finite-volume formulations are used to solve the full-potential equation for the irrotational part of the flowfield. The finite-difference formulation is based on a generalized coordinate transformation [3,4], while the finite-volume formulation is based on mass flux balance [5]. General nonconservative, partially conservative and fully conservative artificial viscosities and shock-point operators, as described in Ref. 3, are applied to reflect the directional bias of local supersonic flows. The rotational part of the flowfield is determied from the momentum equation.

A brief overview of Euler correction methods is given in Section 2.0. The finite-difference and finite-volume formulations of the full-potential equation are described in Section 3.0. The Clebsch formulation of the rotational velocity components is described in Section 4.0. The numerical procedure and results for two- and three-dimensional flows are described in Sections 5.0 and 6.0, respectively. Concluding remarks are given in Section 7.0.

2.0 OVERVIEW

The Euler correction methods which produce Euler-like solutions can be classified into three categories according to their degree of approximation. The first simply accounts for the total pressure and density losses across the shocks. The total pressure is computed downstream of the shock and remains constant along streamlines. Because of a total density jump across the shock, the governing equation at shock points is significantly modified, while the governing equation downstream of the shock point is slightly modified due to the variation of total density between streamlines. The total pressure downstream of the shock is computed according to the Rankine-Hugoniot shock relation, and no additional equation is needed for its solution. Because the vorticity downstream of shocks has only third-order effects on the solutions in the transonic region, this approach generally predicts shocks agreeing well with Euler solutions than either full conservative or nonconservative schemes.

Several investigators have developed schemes in this category, including Hafez and Lovell [6], and Klopfer and Nixon [7]. The partially conservative schemes developed by Lock [8] and Chen [9] are also included in this category, because the addition of a mass source at shock points in the partially conservative schemes is similar to the correction of total density downstream of the shock. In addition, the total pressure loss downstream of the shock can significantly affect the Kutta condition. For example, Chen, Clark and Vassberg [10] showed that by imposing the nonisentropic Kutta condition, the computed shocks agree fairly well with the Euler solutions, even for strong shock cases.

The second kind of Euler correction method decomposes the velocity vector into potential and rotational components. The rotational component is explicitly related to the vorticity field downstream of the shock. There are different ways to decompose the velocity vector. Brown, Brecht and Walsh [11] simply add a scalar function to the streamwise velocity component. Sokhey [12] and Hafez and Lovell [6] apply Helmholtz theory to decompose the velocity vector into irrotational and the rotational components such that the stream function can be used to compute the vorticity. Ecer and Akay [13,14] apply the Clebsch transformation to define the rotational velocity component in conjunction with the use of a finite-element method. This kind of Euler correction method is more general than the first method and additional governing equations are

applied to solve for the rotational velocity components. The additional equations for the rotational part which govern the convection of the vorticity are hyperbolic, and require a relatively small amount of computational time to solve.

The third kind of Euler correction method, proposed by T.C. Tai [15], is a hybrid method which combines a finite-difference relaxation method with the method of integral relations. The Euler equations in integral form are solved downstream of the shock. Both the shock location and circulation are continuously updated during the iterations until the far downstream and the Kutta condition are satisfied. Most of the works cited above are for two-dimensional analysis, except the works of Ecer [14].

The present method applies the Clebsch transformation as the method of Ecer and Akay, except that in the present method the finite-difference/finite-volume full-potential method is applied to solve for the irrotational part and also that different Clebsch variables are chosen. Both the two- and three-dimensional full-potential methods are well developed, and the extension of these methods to include the rotational velocity components is straightforward. Furthermore, the multigrid scheme developed for the full-potential methods works equally well in the present method despite the additional equations for rotational velocity components.

A preliminary description of the present method and results is given in Ref. 16. Both the two- and three-dimensional methods are described in more detail in the following sections. Solutions are presented for various airfoils, wings and wing/bodies, including an F-14 wing/body, and comparisons are made with both the full potential and time marching Euler solutions when available.

3.0 FINITE-VOLUME VERSUS FINITE-DIFFERENCE FORMULATION

Both the finite-difference formulation of Chen [3,4] and the finite-volume formulation of Jameson and Caughey [5] are used in the present method to solve the full-potential equation for the irrotational part of the flowfield. In the finite-difference formulation, the full-potential equation written in general coordinates is employed; since a quadratic coordinate transformation is applied, the odd- and even-point solutions are naturally coupled together. In the finite volume formulation, the density term is explicitly computed from the potential function distribution, and fluxes through cell surfaces are conserved. However, coupling terms are needed to add to the finite volume formulation to avoid the decoupling of odd- and even-point solutions. The finite-difference formulation is described in Section 3.1, the finite-volume formulation in Section 3.2, and artificial viscosities and shock-point operators are described in Section 3.3.

3.1 Finite-Difference Method

The full-potential equation can be expressed as

$$(a^2 - u^2)\phi_{xx} + (a^2 - v^2)\phi_{yy} + (a^2 - w^2)\phi_{zz} - 2uv\phi_{xy} - 2vw\phi_{yz} - 2uw\phi_{xz} = 0 \quad (1)$$

where u, v, w are the x, y, z components of the flow velocity, respectively, and a is the local speed of sound determined from the energy equation

$$a^2 = a_o^2 - \frac{\gamma - 1}{2}(u^2 + v^2 + w^2) \quad (2)$$

where γ is the ratio of specific heats for the assumed calorically perfect gas an a_o is the stagnation speed of sound.

After performing the matrix inversion, multiplication, and algebraic manipulation, a transformed full-potential equation multiplied by the determinant of the Jacobian transformation matrix, D, in general curvilinear coordinates can be derived as [3,4]

$$c_1\phi_{xx} + c_2\phi_{yy} + c_3\phi_{zz} + c_4\phi_{xy} + c_5\phi_{yz} + c_6\phi_{xz} + c_7\phi_x + c_8\phi_y + c_9\phi_z = 0 \quad (3)$$

where

$$c_1 = [a^2(h_1^2 + h_2^2 + h_3^2) - U^2]/D \quad (4)$$

$$c_2 = [a^2(h_4^2 + h_5^2 + h_6^2) - V^2]/D \quad (5)$$

$$c_3 = [a^2(h_7^2 + h_8^2 + h_9^2) - W^2]/D \quad (6)$$

$$c_4 = [2a^2(h_1h_4 + h_2h_5 + h_3h_6) - 2UV]/D \quad (7)$$

$$c_5 = [2a^2(h_4h_7 + h_5h_8 + h_6h_9) - 2VW]/D \quad (8)$$

$$c_6 = [2a^2(h_1h_7 + h_2h_8 + h_3h_9) - 2UW]/D \quad (9)$$

$$c_7 = -(h_1p_X + h_2p_Y + h_3p_Z)/D \quad (10)$$

$$c_8 = -(h_4p_X + h_5p_Y + h_6p_Z)/D \quad (11)$$

$$c_9 = -(h_7p_X + h_8p_Y + h_9p_Z)/D \quad (12)$$

U, V, W are velocity components defined as

$$U = h_1u + h_2v + h_3w \quad (13)$$

$$V = h_4u + h_5v + h_6w \quad (14)$$

$$W = h_7u + h_8v + h_9w \quad (15)$$

Coefficients $h_1 \ldots h_9$ are transformation derivatives defined as

$$h_1 = y_Yz_Z - y_Zz_Y \quad (16)$$

$$h_2 = z_Yx_Z - z_Zx_Y \quad (17)$$

$$h_3 = x_Yy_Z - x_Zy_Y \quad (18)$$

$$h_4 = y_Zz_X - y_Xz_Z \quad (19)$$

$$h_5 = z_Zx_X - z_Xx_Z \quad (20)$$

$$h_6 = x_Zy_X - x_Xy_Z \quad (21)$$

$$h_7 = y_Xz_Y - y_Yz_X \quad (22)$$

$$h_8 = z_Xx_Y - z_Yx_X \quad (23)$$

$$h_9 = z_Xy_Y - x_Yy_X \quad (24)$$

and coefficients p_X, p_Y, and p_Z are second-order transformation derivatives defined as

$$p_X = c_1 x_{XX} + c_2 x_{YY} + c_3 x_{ZZ} + c_4 x_{XY} + c_5 x_{YZ} + c_6 x_{XZ} \tag{25}$$

$$p_Y = c_1 y_{XX} + c_2 y_{YY} + c_3 y_{ZZ} + c_4 y_{XY} + c_5 y_{YZ} + c_6 y_{XZ} \tag{26}$$

$$p_Z = c_1 z_{XX} + c_2 z_{YY} + c_3 z_{ZZ} + c_4 z_{XY} + c_5 z_{YZ} + c_6 z_{XZ} \tag{27}$$

The determinant of the Jacobian transformation matrix is defined as

$$D = h_1 x_X + h_4 x_Y + h_7 x_Z \tag{28}$$

The velocity components u, v, w are defined as

$$u = (h_1 \Phi_X + h_4 \Phi_Y + h_7 \Phi_Z)/D \tag{29}$$

$$v = (h_2 \Phi_X + h_5 \Phi_Y + h_8 \Phi_Z)/D \tag{30}$$

$$w = (h_3 \Phi_X + h_6 \Phi_Y + h_9 \Phi_Z)/D \tag{31}$$

A second-order local coordinate transformation which transforms a 27-point cell from the physical space to the computational space (Fig. 1) can be applied to formulate a second-order finite-difference approximation to Eq. (3) as described in Ref. 3.

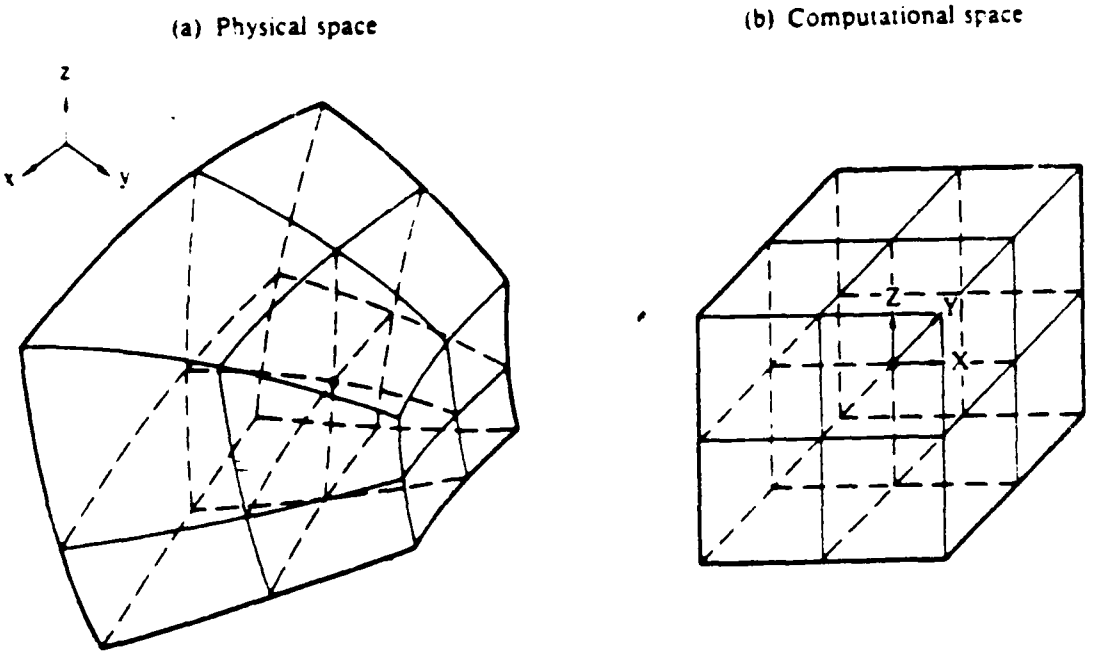

Figure 1. Transformation of a second-order element.

Equation (3) can be reduced to a two-dimensional equation:

$$c_1\Phi_{XX} + c_2\Phi_{YY} + c_4\Phi_{XY} + c_7\Phi_X + c_8\Phi_Y = 0, \tag{32}$$

with c_1, c_2, c_4, c_7, and c_8 redefined as

$$c_1 = [a^2(x_Y^2 + y_Y^2) - U^2]/D^2 \tag{33}$$

$$c_2 = [a^2(x_X^2 + y_X^2) - V^2]/D^2 \tag{34}$$

$$c_2 = -2[a^2(x_X x_Y + y_X y_Y) - UV]/D^2 \tag{35}$$

$$c_7 = (x\, p_Y - y_Y p_X)/D \tag{36}$$

$$c_8 = (y_X p_X - x_X p_Y)/D \tag{37}$$

and U, V, u, v, D, p_X, and p_Y redefined as

$$U = uy_Y - vx_Y \tag{38}$$

$$V = uy_X - vx_X \tag{39}$$

$$u = (y_Y\Phi_X - y_X\Phi_Y)/D \tag{40}$$

$$v = (x_X\Phi_Y - x_Y\Phi_X)/D \tag{41}$$

$$D = x_X y_Y - x_Y y_X \tag{42}$$

$$p_X = c_1 x_{XX} + c_2 x_{YY} + c_3 x_{XY} \tag{43}$$

$$p_Y = c_1 y_{XX} + c_2 y_{YY} + c_3 y_{XY} \tag{44}$$

Equation (32) is consistent with the two-dimensional equation derived in Ref. 17. The detail of the finite-difference approximation to Eqs. (3) and (32) can be found in Refs. 3 and 4.

3.2 Finite-Volume Method

The finite-volume method of Jameson and Caughey [5] applies the mass flux conservation principle to formulate the finite-difference approximation to the full-potential equation. As shown in Fig. 2 for a two-dimensional case, four primary cells, 1298, 2349, 9456 and 8967, surrounding the control point 9 are

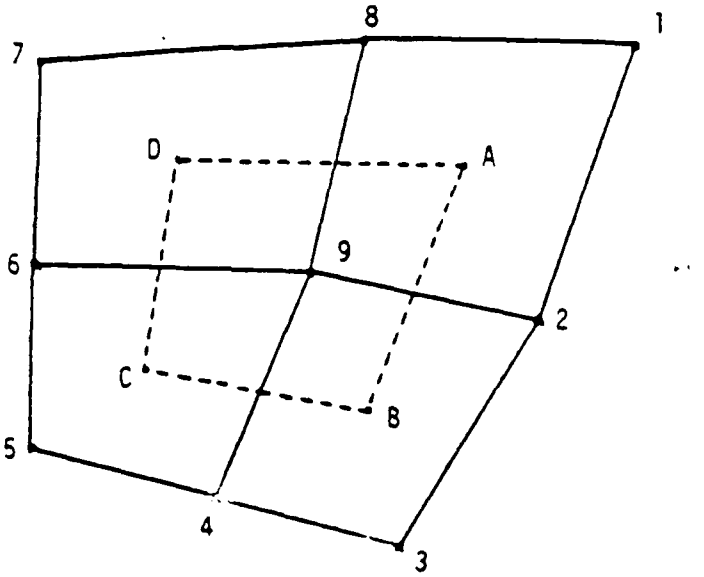

Figure 2. Primary and secondary cells in the finite-volume scheme.

first used to evaluate the flow properties including the velocity components. Then the conservation of mass flux is applied along the four cell boundaries of the secondary cell ABCD which is formed by the centers of the primary cells. The evaluation of the mass flux on these four secondary cell surfaces introduces a "lumping" error in the finite-difference approximation of the full-potential equation at the control point 9. In addition, the finite-difference approximation thus constructed results in uncoupling of even- and odd-point solutions. The remedy to this problem is to add proper coupling terms, which essentially shifts the evaluation of mass fluxes from the centers of four primary cells to the control point 9. As derived in Eqs. (33) and (34), the coefficients c_1 and c_2 are the leading terms of second derivatives of the potential function in the X and Y direc- tions, respectively. The following coupling term with a cross derivative

$$A_X = \frac{1}{2}\,[a^2(x_Y^2 + y_Y^2) - U^2]\Phi_{XY} \tag{45}$$

compensates for the lumping error in computing the flux balance in the X-direction. Similarly the following coupling term with a cross derivative

$$A_Y = \frac{1}{2}\,[a^2(x_X^2 + y_X^2) - V^2]\Phi_{XY} \tag{46}$$

compensates for the lumping error in computing the flux balance in the Y-direction. Similar coupling terms can be constructed for three-dimensional cases.

With these coupling terms, the finite-difference approximation of the finite-volume method is very similar to that of the finite-difference method described in Section 3.1 The approximation of the coupling terms in the finite-volume method is identical to the exact coupling term in the finite-difference method only if the mesh lines are perpendicular to each other. However, since the leading terms of the second derivatives of the two methods are identical, the relaxation scheme can be commonly constructed and shared by both methods while allowing different ways of computing the residuals. In the method of Jameson and Caughey [5], the coupling terms are constructed in divergence form. Therefore, their scheme is fully conservative. Although the finite-difference method has an exact coupling of even- and odd-point solutions, the method is not fully conservative.

Both the finite-difference and the finite-volume methods are implemented in the present study. A comparison of the solutions obtained by the two methods is given in Section 6.1.

3.3 Artificial Viscosities and Shock-Point Operators

The second derivative of the potential function in the streamwise direction, S, is given as

$$\Phi_{SS} = \frac{a^2}{q^2}\left(u^2\Phi_{xx} + v^2\Phi_{yy} + w^2\Phi_{zz} + 2uv\Phi_{xy} + 2vw\Phi_{yz} + 2uw\Phi_{xz}\right) \tag{47}$$

Equation (47) can be rewritten as

$$\Phi_{SS} = \frac{1}{q^2}\left(U^2\Phi_{XX} + V^2\Phi_{YY} + W^2\Phi_{ZZ} + 2UV\Phi_{XY} + 2VW\Phi_{YZ} + 2UW\Phi_{XZ}\right) \tag{48}$$

where U, V, W are given in Eqs. (13) through (15).

The directional bias of supersonic flows can be properly simulated by performing an upwind differencing or adding artificial viscosities in the approximate streamwise direction. If Y = constant lines are in the approximate s direction, the principal part of Φ_{SS} can be approximated by

$$\Phi_{SS} \approx \frac{U^2}{q^2}\Phi_{XX} \tag{49}$$

A first-order artificial viscosity can be expressed by

$$H = (\Delta X)\left[\frac{\mu U^2 \Phi_{XX}}{D}\right]_X = \left(\frac{\mu U^2 \Phi_{XX}}{D}\right)_{I-1} - \left(\frac{\mu U^2 \Phi_{XX}}{D}\right)_I \tag{50}$$

where

$$\mu = \max\left(1 - \frac{a^2}{q^2}, 0\right) \tag{51}$$

H is then added to the finite-difference representation of Eq. (3) at supersonic points. At shock points, i.e., the first downstream subsonic points after the shocks, the following first-order artificial viscosity H_s is added with p_m controlling the nonconservative differencing:

$$H_s = (p_m - 1)\left(\frac{\mu U^2 \Phi_{XX}}{D}\right)_{I-1} \tag{52}$$

If $p_m = 0$, the quantity $\mu U^2 \Phi_{XX}$ is conserved along Y = constant lines, implying that the added artificial viscosities are conserved along approximate streamlines. If $p_m > 0$, a numerical mass flux is introduced at shocks, modifying the locations and strengths of the shocks. The effect of p_m on the captured shocks will be discussed later. A second-order artificial viscosity and shock-point operator can be expressed as

$$H = (\Delta X)^2 \left[\frac{\mu U^2 \Phi_{XX}}{D}\right]_{XX} = \left(\frac{\mu U^2 \Phi_{XX}}{D}\right)_{I-2} - 2\left(\frac{\mu U^2 \Phi_{XX}}{D}\right)_{I-1} + \left(\frac{\mu U^2 \Phi_{XX}}{D}\right)_I \tag{53}$$

$$H_s = (p_m - 1)\left[\frac{(\Delta X)\mu U^2 \Phi_{XX}}{D}\right]_X = \left[\left(\frac{\mu U^2 \Phi_{XX}}{D}\right)_{I-1} - \left(\frac{\mu U^2 \Phi_{XX}}{D}\right)_{I-2}\right](p_m - 1) \tag{54}$$

The solution is second-order accurate at both subsonic and supersonic points, and first-order accurate at shock points. Although μ is a ramp function, both H and H_s reduce to zero as the mesh size goes to zero. In the so-called quasi-conservative schemes, the finite-difference formulation, described in Section 3.1, is applied, and only the differencing of artificial viscosities is in divergence form; the differencing of the governing potential equation is not. A second-order fully conservative scheme also can be constructed by incorporating H and H_s into the finite-volume formulation described in Section 3.2.

Similarly, a nonconservative scheme can be developed by adding the following artificial viscosity at supersonic points

$$H = \left(\frac{\rho U^2}{D}\right)_i \left[(\Phi_{XX})_{i-1} - (\Phi_{XX})_i\right] \tag{55}$$

to make the differencing upwind as in the original Murman and Cole scheme [18], while no artificial viscosity is added at the shock point.

4.0 CLEBSCH TRANSFORMATION

The Clebsch transformation has been extensively employed in the calculation of three-dimensional rotational flows in turbomachines up to the subcritical flow range using mostly analytical approaches. The method has been successfully developed for computing shear flows [19,20], wake flows [21,22,23], and non-axisymmetric inlet flows [24].

In the Clebsch formulation of steady rotational flows, the velocity vector $\underset{\sim}{V}$ is decomposed into a potential part and rotational parts, written in terms of scalar functions [19]:

$$\underset{\sim}{V} = \nabla\phi + \sum_n \sigma_n \nabla\lambda_n \tag{56}$$

Hence, by definition, the vorticity vector $\underset{\sim}{\Omega}$ is nonzero:

$$\underset{\sim}{\Omega} \equiv \nabla \times \underset{\sim}{V} = \sum_n \nabla\sigma_n \times \nabla\lambda_n \tag{57}$$

To determine the flowfield, the Clebsch variables ϕ, σ_n and λ_n must be chosen so that the equations of motion are satisfied. In general, each pair of σ_n and λ_n can be considered to represent the vorticity field generated by various shocks or the trailing vorticity downstream of lifting bodies such as wings or propeller blades.

For steady flow,

$$\nabla \cdot (\rho \underset{\sim}{V}) = 0 \tag{58}$$

while the momentum equation, written in Lamb's form for isoenergetic flow in the absence of body forces, is

$$\underset{\sim}{V} \times \underset{\sim}{\Omega} = -\frac{a^2}{\gamma} \nabla s \tag{59}$$

where ρ is the density, s the entropy, a the speed of sound, and γ the ratio of the specific heats of the flow.

In the present approach, the potential part in Eq. (56) is determined by solving the full-potential equation given in the previous section, while the rotational parts in Eq. (56) are chosen to satisfy the momentum equation, Eq. (59). The entire flowfield can then be computed by solving the governing coupled equations of these Clebsch variables iteratively.

When shocks appear in the flowfield, entropy increases across the shocks. The rotational parts of the velocity vector defined in Eq. (56) are determined from the momentum equation. A general solution to Eq. (59) is given by:

$$\underset{\sim}{\Omega} = \underset{\sim}{\Omega}_H + \underset{\sim}{\Omega}_p \tag{60}$$

Here $\underset{\sim}{\Omega}_H$ is the homogeneous solution of Eq. (59), namely:

$$\underset{\sim}{V} \times \underset{\sim}{\Omega}_H = 0 \tag{61}$$

and $\underset{\sim}{\Omega}_p$ is the particular solution of Eq. (59), namely:

$$\underset{\sim}{V} \times \underset{\sim}{\Omega}_p = -\frac{a^2}{\gamma} \nabla s \tag{62}$$

The particular solution $\underset{\sim}{\Omega}$ represents the vorticity component which is not parallel to the velocity vector.

Following arguments similar to those in Refs. 19 to 24, the vorticity component associated with the entropy jump across shocks can be expressed as:

$$\underset{\sim}{\Omega}_p = \nabla\tau \times \nabla s \tag{63}$$

where s is the entropy field and τ is a Clebsch variable. Substituting Eq. (62) into Eq. (61), and considering that entropy is convected along streamlines behind shocks,

$$\underset{\sim}{V} \cdot \nabla s = 0 \tag{64}$$

it can be shown that the governing equation for τ is

$$\underset{\sim}{V} \cdot \nabla\tau = \frac{a^2}{\gamma} \tag{65}$$

The Clebsch variable τ is similar to the Darwin-Lighthill-Hawthorne drift function [19]. The variation of τ from streamline to streamline is directly connected to the stretching and tipping of the vortex filaments associated with the entropy variation in the flowfield.

The homogeneous solution represents the vorticity component which is parallel to the velocity vector. For the problem considered here, $\underset{\sim}{\Omega}_H$ is the trailing vorticity shed behind a wing. In the airfoil case, $\underset{\sim}{\Omega}_H$ is identically zero. It can be shown that the homogeneous solution is

$$\underset{\sim}{\Omega}_H = \delta(\xi)\nabla\xi \times \nabla\Gamma \tag{66}$$

where $\xi \equiv y - f(x,z) = 0$ defines the wake surface or the location of the trailing vortex sheet, $\delta(\xi)$ is the Dirac delta function, and Γ is the circulation of the vortex filaments shed by the wing. Note that according to Eq. (66), the trailing vorticity lies in the wake surface and is zero everywhere except on the wake surface. Substituting Eq. (66) into Eq. (61), along with the use of the wake boundary condition, namely:

$$\underset{\sim}{V}_w \cdot \nabla\xi = 0 \tag{67}$$

the condition for zero pressure jump across the wake, including the trailing edge, is obtained

$$\underset{\sim}{V}_w \cdot \nabla\Gamma = 0 \tag{68}$$

Here $\underset{\sim}{V}_w$ is the mean velocity between the wake upper and lower sides.

Given the velocity field from the previous iteration step, the Clebsch variables s, τ, ξ and Γ can be updated by solving Eqs. (64), (65), (67) and (68), respectively.

As mentioned earlier, the full-potential equation is employed to determine the potential part of the velocity vector. Using the results derived in Section 2.1, the velocity vector can be written as:

$$\underset{\sim}{V} = \nabla\phi - s\nabla\tau + H(\xi)\nabla\Gamma \tag{69}$$

where $H(\xi)$ is the step function. Substituting Eq. (69) into Eq. (58) yields

$$\nabla \cdot \{\rho[\nabla\phi - s\nabla\tau + H(\xi)\nabla\Gamma]\} = 0 \tag{70}$$

Given the rotational parts from the previous iteration step, the potential part can be updated by solving Eq. (70) in the following form:

$$\nabla \cdot \{\rho\nabla\phi\} = -\nabla \cdot \{\rho(-s\nabla\tau + H(\xi)\nabla\Gamma)\} \tag{71}$$

The density ρ can be related to the local flow properties by means of the isentropic relation and the energy equation:

$$\rho = e^{-s}(M_\infty^2 a^2)^{1/(\gamma-1)} \tag{72}$$

and

$$a^2 = \frac{1}{M_\infty^2} + \frac{\gamma - 1}{2}(1 - q^2) \qquad (73)$$

where q is the magnitude of the velocity vector, and M_∞ is the freestream Mach number.

5.0 NUMERICAL PROCEDURE AND RESULTS FOR TWO-DIMENSIONAL FLOWS

The governing equations and boundary condition, the numerical procedures to solve them and the results for two-dimensional flows are presented in this section.

5.1 Governing Equations

The finite-difference and finite-volume methods can now be modified to include the effects of the total pressure loss across shocks and the vorticity downstream of shocks. For flow around an airfoil, there is no trailing wake downstream of the trailing edge. From Eqs. (40), (41) and (69), and applying the same coordinate transformation as in Section 2.0, the velocity components can be expressed as

$$u = [(y_Y\Phi_X - y_X\Phi_Y) - s(y_Y\tau_X - y_X\tau_Y)]/D$$
$$v = [(x_X\Phi_Y - x_Y\Phi_X) - s(x_X\tau_Y - x_Y\tau_X)]/D \tag{74}$$

and the governing equations can be expressed as

$$C_1\Phi_{XX} + C_2\Phi_{YY} + C_4\Phi_{XY} + C_7\Phi_X + C_8\Phi_Y = Da^2\nabla\cdot(\rho\nabla\tau)/\rho \tag{75}$$

with the following two equations for solving the Clebsch variables s and τ:

$$Us_X + Vs_Y = 0 \tag{76}$$

$$U\tau_X + V\tau_Y = D\frac{a^2}{\gamma} \tag{77}$$

A multigrid line-relaxation scheme, originally developed for transonic full-potential methods [24-28] is applied to solve Eq. (75) for the potential function Φ, along with the new expression, Eq. (74), to compute the velocity components. The Clebsch variables can be solved analytically under certain approximations, or numerically by using the Lax-Wendroff scheme [29].

5.2 Approximate Euler Clebsch Approach

The flowfield around an airfoil can be divided into irrotational and rotational regions as shown in Fig. 3. The flowfield downstream of the shock is rotational. Across a shock, there is an entropy jump which can be estimated from the Rankine-Hugoniot shock relation if the Mach number upstream of the shock is known. The entropy s is then convected downstream along the streamlines as

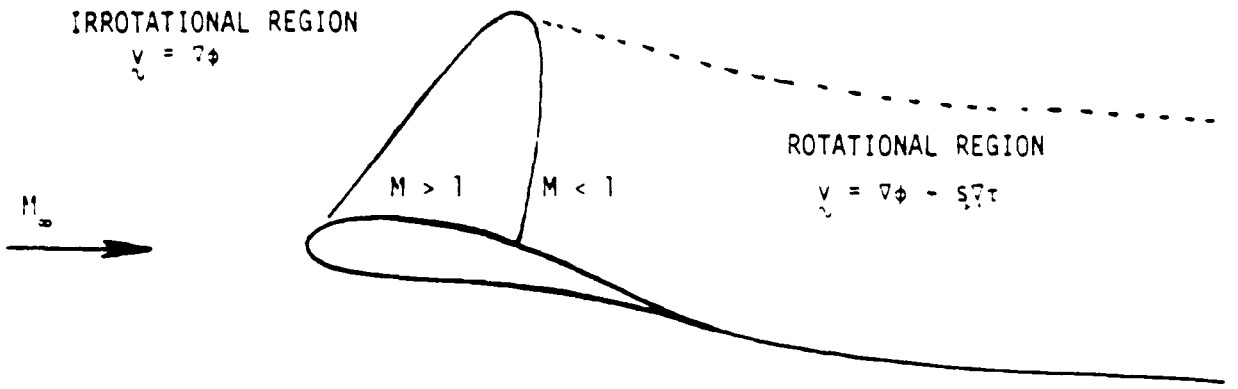

Figure 3. Irrotational and rotational flowfield about an airfoil.

described in Eq. (76). In the present method, a C-mesh which conforms to the airfoil surface is applied. Therefore, it is a fairly good approximation that the entropy is constant along the mesh lines Y = constant downstream of the shock.

A second approximation can be made in order to solve for the Clebsch variable τ analytically. As described in Section 4.0, τ represents a material coordinate surface which stretches according to the local flow velocity, as described in Eq. (77). If the velocity is assumed to be freestream velocity, and the speed of sound is also assumed to be freestream value, Eq. (77) can be rewritten as

$$(\cos\alpha)\,\frac{\partial\tau}{\partial x} + (\sin\alpha)\,\frac{\partial\tau}{\partial y} = \frac{1}{\gamma M_\infty^2} \tag{78}$$

where α is the angle of attack.

In order to solve Eq. (78), boundary conditions need to be prescribed for τ at the shock front. Since the potential function ϕ is taken to be continuous across the shock, the conservation of tangential momentum across the shock front requires τ to be a constant everywhere on the shock surface. However, since the Clebsch variable τ itself is not used in the present formulation to compute the velocity, but rather its gradient, the boundary condition is enforced by requiring that the jump in the velocity vector across the shock is normal to the shock surface. Since all the jump in the velocity across the

shock is contained in the rotational part, this condition is satisfied by the following:

$$\nabla\tau \times \hat{n} = 0 \tag{79}$$

where $\hat{n} \equiv (n_x)\hat{e}_x + (n_y)\hat{e}_y$ defines the local shock surface unit normal. Solving Eqs. (78) and (79) simultaneously for the gradient of τ gives, in the two-dimensional case,

$$\nabla\tau = \frac{\hat{n}}{\gamma M_\infty^2 (n_x \cos\alpha + n_y \sin\alpha)} \tag{80}$$

Hence, in the 2-D Euler correction method, the velocity vector reduces to

$$\underset{\sim}{V} = \nabla\phi - \frac{s}{\gamma M_\infty^2 (n_x \cos\alpha + n_y \sin\alpha)} \hat{n} \tag{81}$$

Since $\nabla\tau$ is constant along Y = constant lines, the source term on the right-hand side of Eq. (75) is small everywhere except at shock points where discontinuities in s and ρ exist.

To obtain the flowfield, the following iterative procedure is employed:

1. Set the initial solution for ϕ to be the freestream condition, and set s and τ to be zero.

2 Solve Eq. (75) for ϕ using the multigrid relaxation method.

3. Obtain the shock surface normal vector and the entropy jump across the shocks from the Rankine-Hugoniot relation when supersonic pockets (or shocks) start to appear in the flowfield.

4. Update the rotational part in Eq. (81).

5. Repeat Steps 2 to 5 until solutions converge.

5.3 Exact Euler-Clebsch Approach

The governing equations for s and τ, Eqs. (76) and (77), are of hyperbolic type. They can be solved using the second-order Lax-Wendroff explicit scheme.

Consider the following general equation:

$$U \frac{\partial F}{\partial X} + V \frac{\partial F}{\partial Y} = G \tag{82}$$

where $F \equiv (s, \tau)$ and $G \equiv (0, a^2/\gamma)$.

The solution procedure to solve the above equation consists of prescribing the initial condition for F at the shock front, and solving Eq. (82) by marching downstream in the X direction. During space marching, the solution of F at the i station is given, and the solution at the (i + 1) station is computed in two steps [29].

Step 1

$$F^{i+1/2}_{j+1/2} = \frac{1}{2}(F^i_{j+1} + F^i_j) - \frac{1}{2}\frac{V_1}{U_1}(F^i_{j+1} - F^i_j) + \frac{1}{2}\frac{G_1}{U_1} \tag{83}$$

$$F^{i+1/2}_{j-1/2} = \frac{1}{2}(F^i_j + F^i_{j-1}) - \frac{1}{2}\frac{V_2}{U_2}(F^i_j - F^i_{j-1}) + \frac{1}{2}\frac{G_2}{U_2} \tag{84}$$

Step 2

$$F^{i+1}_j = F^i_j - \frac{1}{2}\left(\frac{V_1}{U_1} + \frac{V_2}{U_2}\right)\left(F^{i+1/2}_{j+1/2} - F^{i-1/2}_{j-1/2}\right) + \left(\frac{G_1}{U_1} + \frac{G_2}{U_2}\right) \tag{85}$$

The subscripts 1 and 2 denote the cell-centered values of the cells defined in Fig. 4. In this scheme, the Von Neumann stability requires

$$\frac{V}{U} \ll 1 \tag{86}$$

In the flowfield where the scheme applies, the surface normal velocity component is usually small compared with the streamwise component.

The coupling between the potential and rotational solution procedures is similar to the one described in Section 5.1, except in Step 4 where the numerical solutions are computed for s and τ instead of using the analytical solutions.

5.4 Kutta Condition

The Kutta condition requires that the static pressures at the upper and lower trailing edges be matched. Furthermore, it also requires that there is no pressure jump across the streamline emanating from the trailing edge. In the

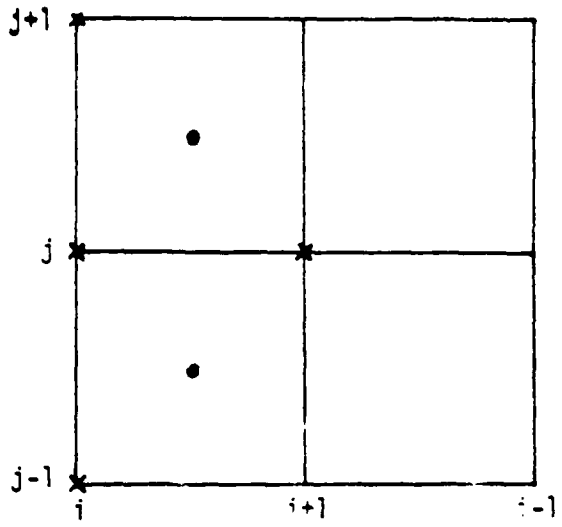

Figure 4. Lax-Wendroff scheme.

full-potential method, flow is assumed to be isentropic everywhere. Therefore the Kutta condition can be satisfied by assuming the potential jump across the trailing edge is constant along the streamline, or the mesh line, emanating from the trailing edge. This ensures that the magnitudes of the velocities on both sides of the streamline are equal, as are the pressures on both sides of the streamline. In the present method if shocks appear on either upper or lower or both surfaces, the total pressures of the streamlines just above and below the trailing edge are different. Hence, in order to have equal pressure across the dividing streamline, the velocity must be discontinuous across it. In this section the velocity discontinuity across this dividing streamline will be shown to come from the rotational term $s\nabla\tau$ so that the condition for ϕ across this dividing streamline is the same as in the full-potential method.

To simplify the derivation, consider the case where there is only one shock on the airfoil upper surface. The static pressure can be written in terms of local velocity and stagnation pressure:

$$p_1 = \left(\frac{p_{t1}}{p_{t2}}\right) \left[1 + \frac{\gamma - 1}{2} M_\infty^2 (1 - q_1^2)\right]^{\gamma/\gamma-1} \tag{87}$$

$$p_2 = \left[1 + \frac{\gamma - 1}{2} M_\infty^2 (1 - q_2^2)\right]^{\gamma/\gamma-1} \tag{88}$$

Equating Eqs. (87) and (88)

$$\left(\frac{p_{t1}}{p_{t2}}\right)\left[1 + \frac{\gamma - 1}{2} M_\infty^2 (1 - q_1^2)\right]^{\gamma/\gamma-1} = \left[1 + \frac{\gamma - 1}{2} M_\infty^2 (1 - q_1^2) - (q - 1)M_\infty^2 q_1 \Delta q - \frac{\gamma - 1}{2} M_\infty^2 \Delta q^2\right]^{\gamma/\gamma-1} \quad (89)$$

where $\Delta q \equiv q_2 - q_1$. Neglecting the term Δq^2 in Eq. (89), an explicit expression for the velocity jump across the dividing streamline can be found.

$$\Delta q = \frac{1}{q_1} \frac{1}{\gamma M_\infty^2}\left[1 - \left(\frac{p_{t2}}{p_{t1}}\right)\right]\left[1 + \frac{\gamma - 1}{2} M_\infty^2 (1 - q_1^2)\right] \quad (90)$$

In practice, the stagnation pressure loss across the shock is generally small even for a strong shock. For example, a shock Mach number of 1.7 results in 15% loss in stagnation pressure. Since Δq is proportional to the stagnation pressure loss, the assumption that the Δq^2 term can be neglected in deriving Eq. (90) is valid.

From Eq. (69), the velocity jump across the dividing streamline is given by

$$\Delta q = \left(s \frac{\partial \tau}{\partial \ell}\right)_1 \quad (91)$$

where ℓ is the distance measured along the dividing streamline.

For isoenergetic flow, the entropy is related to the stagnation pressure by

$$s = 1 - \ell n \left(\frac{p_{t2}}{p_{t1}}\right) \approx 1 - \left(\frac{p_{t2}}{p_{t1}}\right) \quad (92)$$

where, as before, second-order terms in the stagnation pressure loss are neglected.

From the governing equation of the Clebsch variable τ, Eq. (65),

$$\frac{\partial \tau}{\partial \ell} = \frac{1}{q_1} \frac{1}{\gamma M_\infty^2}\left[1 + \frac{\gamma - 1}{2} M_\infty^2 (1 - q_1^2)\right] \quad (93)$$

Substituting Eqs. (92) and (93) into (91),

$$\Delta q = \frac{1}{q_1}\frac{1}{\gamma M_\infty^2}\left[1 - \left(\frac{p_{t2}}{p_{t1}}\right)\right]\left[1 + \frac{\gamma - 1}{2} M_\infty^2 \left(1 - q_1^2\right)\right] \qquad (94)$$

Clearly, Eqs. (90) and (94) are identical. Hence, the Kutta condition can be satisfied by simply keeping the potential jump constant across the mesh line leaving the airfoil trailing edge, as in the full-potential methods. A study of the magnitude of Δq is presented in Fig. 5. Δq expressed in Eq. (94) is plotted versus shock Mach number at freestream Mach number M_∞ = 0.7, 0.75, 0.8 and 0.85. The value of Δq increases as the shock Mach number increases and the freestream Mach number decreases.

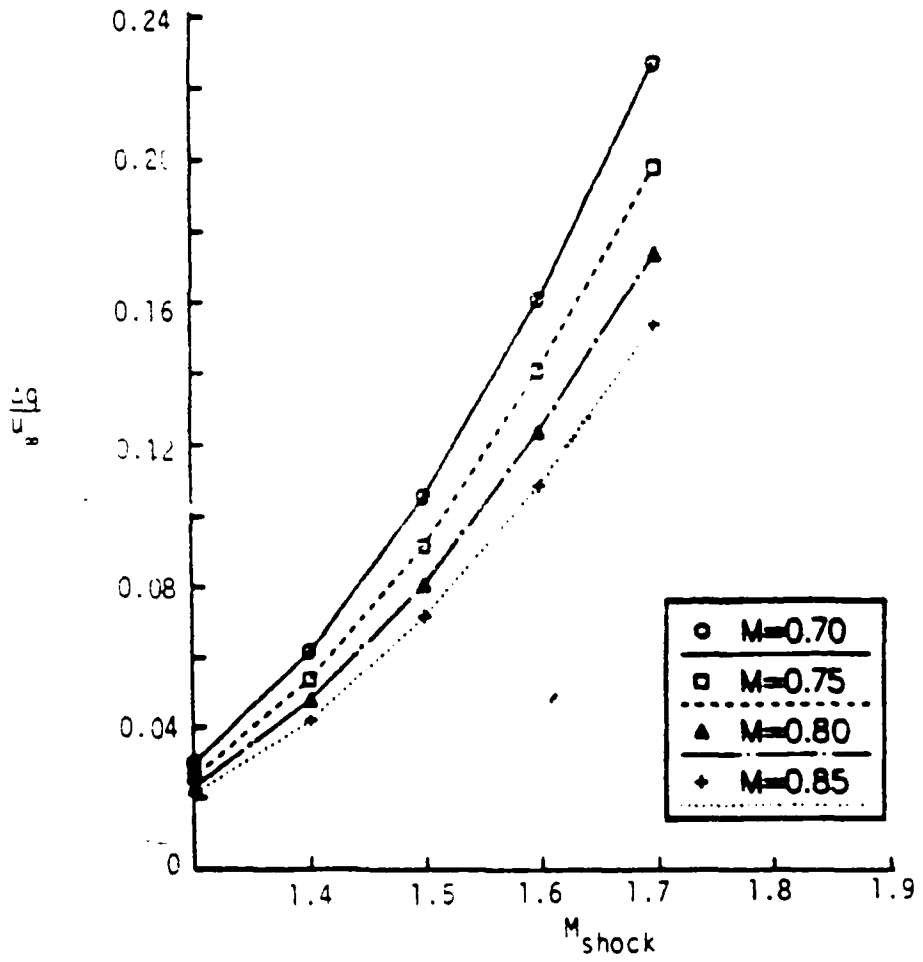

Figure 5. Velocity jump across the wake as described in Eq. (90)

5.5 Numerical Results

The numerical solutions obtained by the present method for airfoils are presented in this section. Figure 6 shows the comparison between the solutions obtained for the NACA-0012 airfoil at $M_\infty = 0.800$ and $\alpha = 1.25°$ from the two Euler-Clebsch approaches and the time-marching Euler method [1]. The fully conservative full-potential solution predicts a shock almost at the trailing edge. The source term in Eq. (75) in the present method accounts for corrections to the total density and the vorticity which are neglected in the full-potential solutions. Solutions obtained by using the approximate and the exact Euler-Clebsch approach predict weaker and more upstream shocks which agree better with the time-marching Euler solution. A study of the order of magnitude on Eqs. (74), (75) and (76) reveals that the first-order correction comes from the source term of Eq. (75) at shock points where entropy jump occurs, and that the second-order correction comes from the vorticity effect which modifies the velocity distribution, Eqs. (74) and (75), and source

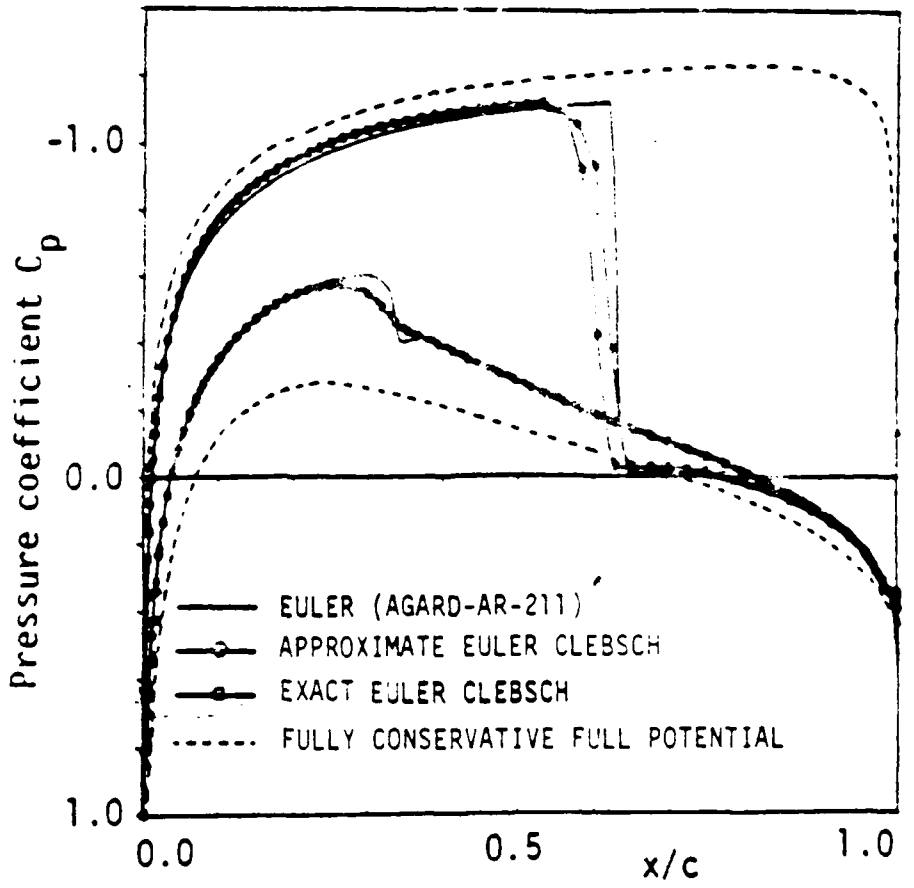

Figure 6. Comparison of solutions for NACA-0012 airfoil at $M_\infty = 0.8$ and $\alpha = 1.25°$.

term of Eq. (76) at points downstream of shock points. In the exact Euler-Clebsch approach, the rotational part is evaluated more accurately, and the solution seems to agree better with the time-marching Euler solution than the approximate Euler-Clebsch solution. Note that the shocks captured by the Euler-Clebsch solutions are not as sharp as those obtained by the time-marching Euler solution, especially on the lower surface. This is probably because the time-marching Euler computation employs more points on the airfoil surfaces than the Euler-Clebsch solutions (192 points vs 162 points).

Figure 7 presents the solutions obtained for the RAE-2822 airfoil at M_∞ = 0.75 and α = 3°. This test case was chosen in order to evaluate the accuracy of the Euler-Clebsch method in the presence of a strong shock. Figure 8 illustrates the stagnation pressure contour obtained using an in-house version

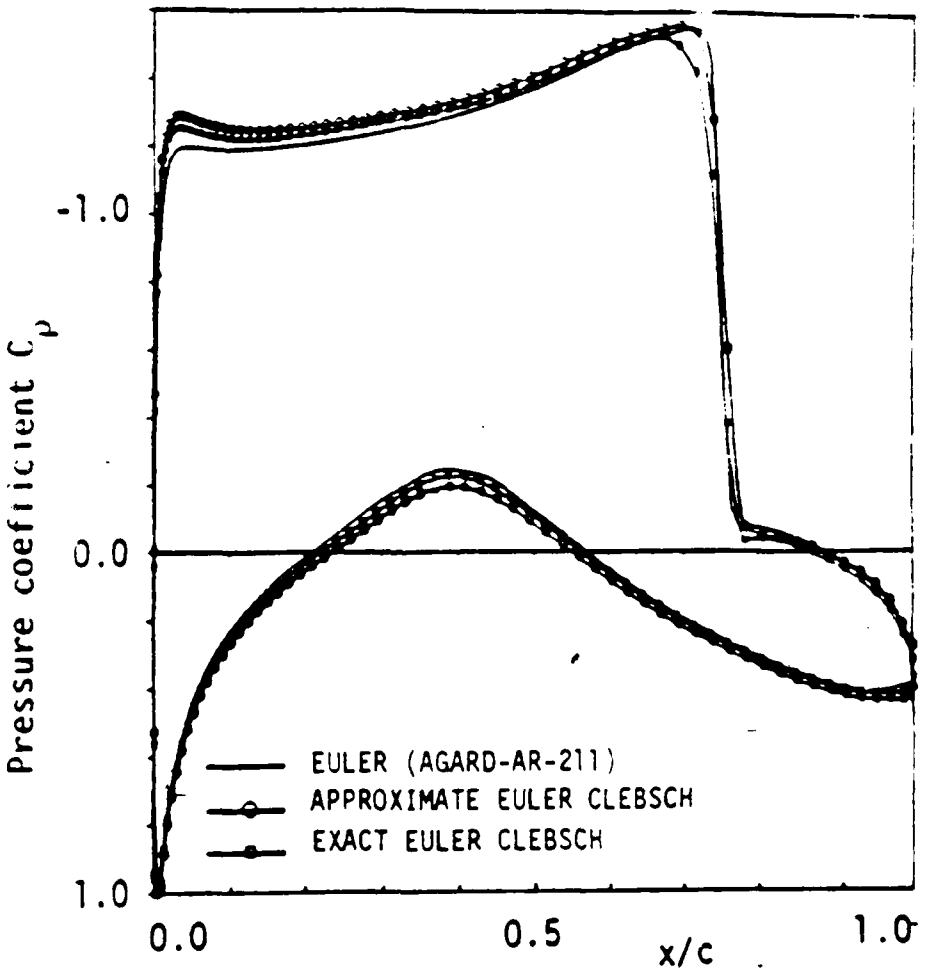

Figure 7. Comparison of solutions for RAE-2822 airfoil at M_∞ = 0.75 and α = 3°.

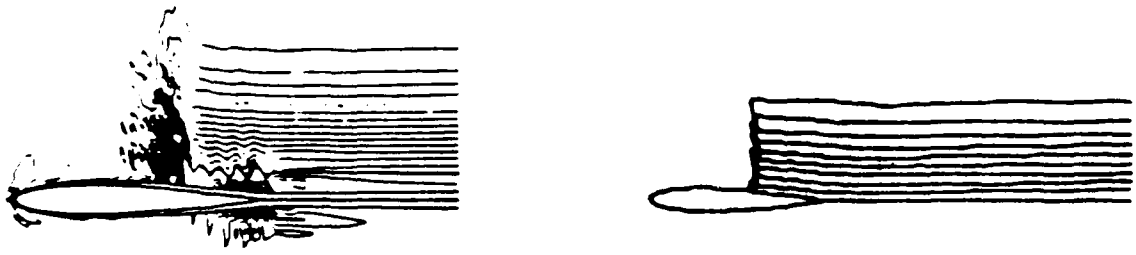

TIME-MARCHING EULER METHOD EULER-CLEBSCH METHOD

Figure 8. Comparison of total pressure contours.

of the Jameson DFLO-53 time-marching Euler method [30,31] and the exact Euler-Clebsch solution. This figure clearly shows that the convective behavior of the stagnation pressure along streamlines is preserved in the present Euler-Clebsch method. The time-marching Euler method, however, has difficulty modeling this inviscid characteristic because of the presence of numerical dissipation terms.

The present exact Euler-Clebsch method, however, has difficulties in giving a converged solution when the shock becomes too strong or the angle of attack becomes too large due to the stability criterion of Eq. (86). More stable schemes such as the Crank-Nicholsen implicit scheme are currently under investigation.

6.0 NUMERICAL PROCEDURE AND RESULTS FOR THREE-DIMENSIONAL FLOWS

The numerical procedure to solve the governing equation with boundary conditions for the three-dimensional flows is discussed in Section 6.1. The numerical results obtained for wings and wing/bodies are presented in the subsequent sections. A comparison of finite-difference and finite-volume solutions is presented in Section 6.2. Both full-potential and Euler-Clebsch solutions obtained for wings are presented in Section 6.3, and the solutions obtained for wing/bodies are presented in Section 6.4.

6.1 Governing Equations

In the three-dimensional case, the approach is similar to the two-dimensional case, except for some additional assumptions and modifications. Only the approximate Euler-Clebsch approach is applied here. First, the wake or the trailing vortex sheet defined by ξ in Eq. (67) is taken to be the grid surface emanating from the wing trailing edge. Furthermore, the trailing vorticity is assumed to be convected along the grid lines leaving the trailing edge. This is done by setting the jump in ϕ across the wake at each spanwise station to be constant along the mesh lines downstream of the trailing edge. Hence, the trailing vorticity is the homogeneous solution defined in Eq. (66). This treatment of the wake is the same as that applied in most potential approaches.

Second, for swept wings, oblique shocks are usually found on most parts of the wing surfaces. In some cases, it is possible to encounter oblique shocks where the total Mach numbers both upstream and downstream of these shocks are supersonic. Although this type of oblique shock does appear in many transonic applications, its shock strength is generally weak; therefore, no entropy correction is given to this type of shock. In the absence of yaw, Eqs. (79)-(81) still hold in 3-D where the local shock surface unit normal vector is defined as $\hat{n} = (n_x)\hat{e}_x + (n_y)\hat{e}_y + (n_z)\hat{e}_z$.

The modified full-potential equation can now be derived from Eqs. (3) and (58) as

$$c_1\phi_{XX} + c_2\phi_{YY} + c_3\phi_{ZZ} + c_4\phi_{XY} + c_5\phi_{YZ} + c_6\phi_{XZ} + c_7\phi_X + c_8\phi_Y + c_9\phi_Z = Da^2\nabla \cdot (\rho s\nabla\tau)/\rho \qquad (95)$$

with the velocity components defined as

$$u = [(h_1\Phi_X + h_4\Phi_Y + h_7\Phi_Z) + s(h_1\tau_X + h_4\tau_Y + h_7\tau_Z)]/D$$
$$v = [(h_2\Phi_X + h_5\Phi_Y + h_8\Phi_Z) + s(h_2\tau_X + h_5\tau_Y + h_8\tau_Z)]/D \quad (96)$$
$$w = [(h_3\Phi_X + h_6\Phi_Y + h_9\Phi_Z) + s(h_3\tau_X + h_6\tau_Y + h_9\tau_Z)]/D$$

In the approximate Euler-Clebsch approach, s is assumed to be constant along τ = constant lines. Following the same argument as in the two-dimensional case, the entropy s can be computed by the Rankine-Hugoniot relation, and the gradient of τ can be approximated by Eq. (80).

In the downstream farfield, the Neumann boundary condition is employed. The implementation of this type of boundary condition requires the knowledge of the far downstream velocity, which is not known a priori and is a function of the shock strength. In the present study, the far downstream velocity, denoted by $\underline{V}_d$, is taken to be

$$\underline{V}_d = (\cos\alpha)\hat{e}_x + (\sin\alpha)\hat{e}_y - \frac{s}{\gamma M_\infty^2 (n_x\cos\alpha + n_y \sin\alpha)}\hat{n} \quad (97)$$

Conceptually, the last term in Eq. (97) is related to the wave drag, and represents the velocity deficit due to the loss in the fluid stagnation pressure across the shock.

6.2 Comparison of Finite-Difference and Finite-Volume Solutions

As described in Section 3.2, two major differences in the finite-difference and the finite-volume methods come from the formulation of the odd- and even-point coupling terms, and the calculation of the density term. The coupling term in the finite-difference method is derived directly from the coordinate transformation, while the coupling term in the finite-volume method accounts for the leading terms only. The explicit calculation of the density term in the finite-volume method makes the scheme conservative, but requires more computational work because of the need to compute exponential quantities.

Figures 9 and 10 present the solutions obtained by the finite-difference and finite-volume methods. The surface boundary condition in the finite-difference method is enforced exactly as it is in the finite-volume method, while different formulations are used in evaluating the residuals. Both solutions are

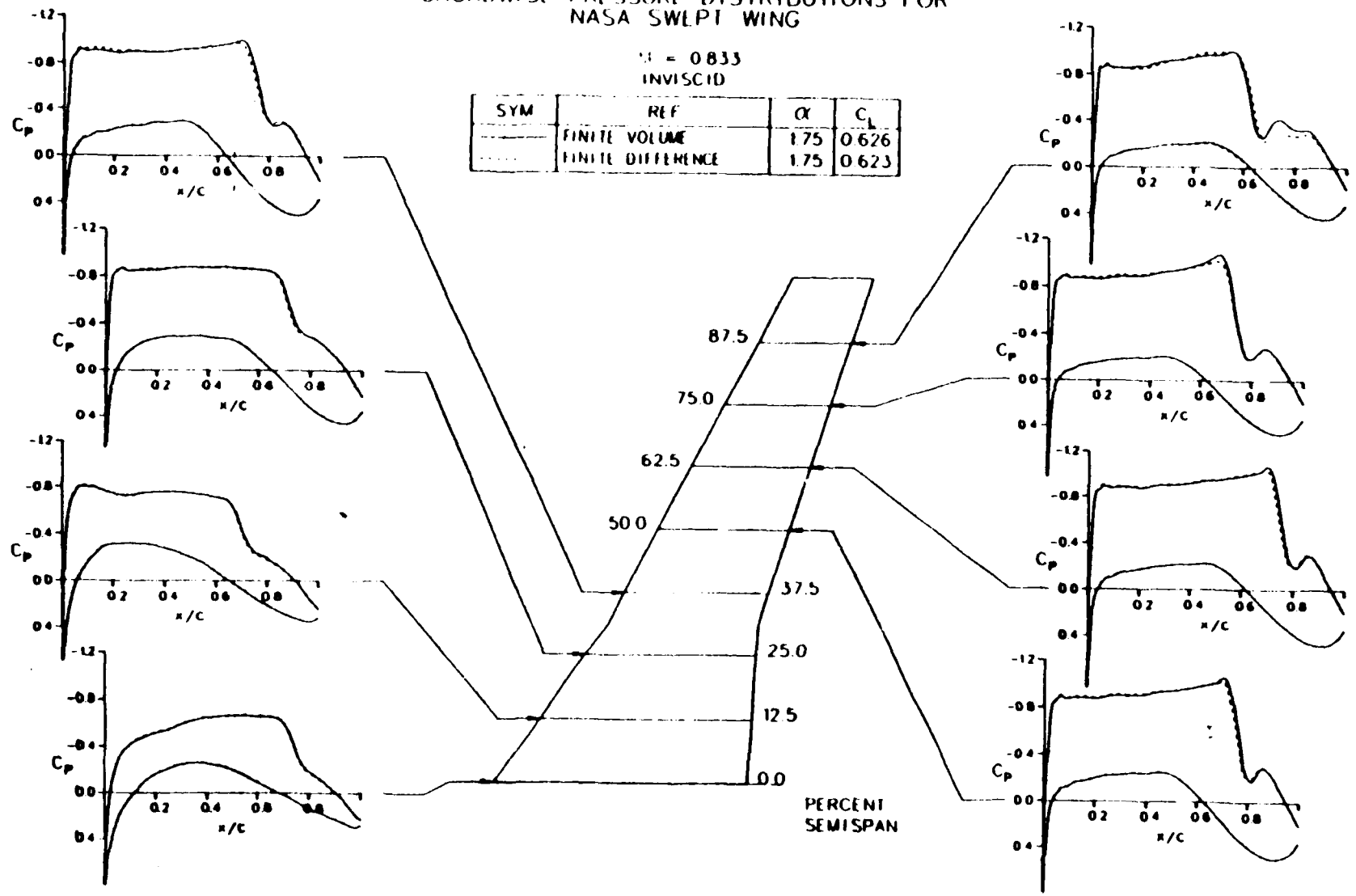

Figure 9. Comparison of finite-difference and finite-volume solutions for a NASA swept wing at M_∞ = 0.833 and α = 1.75°.

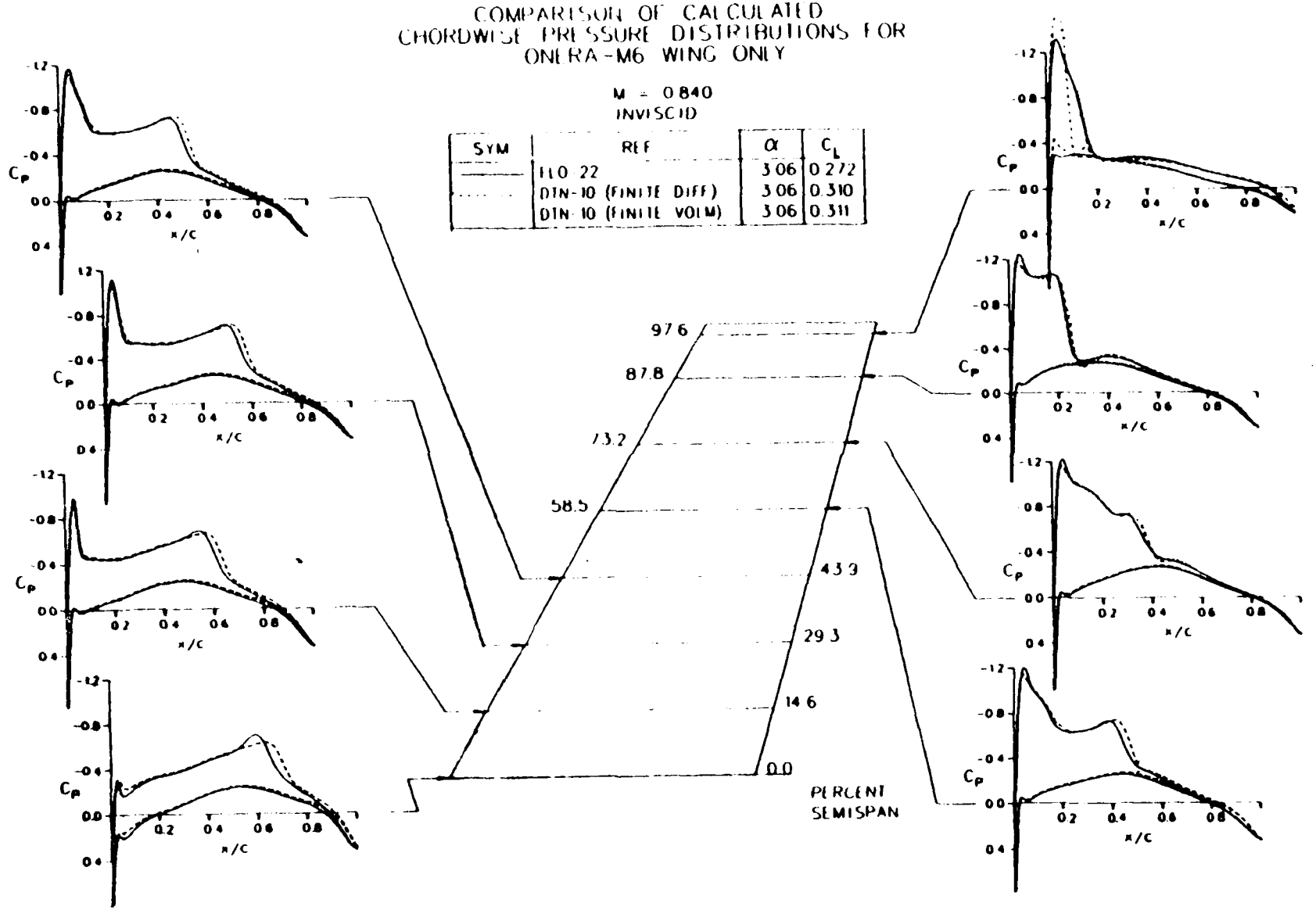

Figure 10. Comparison of finite difference, finite volume and FLO-22 solutions for ONERA M6 wing at M_∞ = 0.84 and α = 3.06°.

obtained using the multigrid scheme. Figure 9 presents two solutions obtained for a NASA swept wing [1] at $M_\infty = 0.833$ and $\alpha = 1.75°$. The finite-difference and finite-volume solutions agree well except for minor differences in the after-shock flow reexpansion near the wing tip. Figure 10 presents a comparison of three computed solutions obtained by the present method and FLO-22 [32] for an ONERA-M6 wing at $M_\infty = 0.84$ and $\alpha = 3.06°$. The nonconservative scheme is applied in the present method in order to make a fair comparison with the FLO-22 solution which is also nonconservative. Both the present finite-volume and finite-difference solutions are obtained using 160 x 24 x 32 mesh points, while the FLO-22 solution is obtained using 192 x 24 x 32 points. The FLO-22 method applies an extrapolated relaxation scheme to accelerate the solution convergence, while the present method applies a multigrid scheme. In general, the present solutions converge better than the FLO-22 solutions. The agreement between the three solutions is generally good, except for a small discrepancy in the prediction of shock locations.

Figure 11 shows a similar comparison of the solutions obtained for a Douglas wind-tunnel model wing, LB-488. The LB-488 wing has a significant aft loading. The present solutions predict an almost flat pressure plateau near the wing root, while FLO-22 predicts a slight oscillation. Most interestingly, both the present finite-volume and finite-difference solutions predict a significant preshock reexpansion between the 65 to 90% semispan locations, while the FLO-22 solution does not. This preshock reexpansion was first observed in the finite-volume solution, and it was uncertain then whether this reexpansion was due to numerical oscillation or possibly due to the special coupling terms described in Section 3.2. The present finite-difference solution obtained with more exact coupling terms still shows the preshock reexpansion. Further investigation with the use of finer meshes should be carried out in order to understand the discrepancy between the present solutions and the FLO-22 solution.

6.3 Euler-Clebsch Solutions

The Euler-Clebsch solutions are obtained using the analytical approach described in Section 6.1. Figures 12 to 14 present the solutions obtained for the NASA swept wing. A comparison of the pressure distributions computed at several spanwise stations using Jameson's time-marching Euler method, the present Euler-Clebsch method, and the nonconservative full-potential method is shown in Fig. 12. This figure clearly demonstrates that the Euler-Clebsch

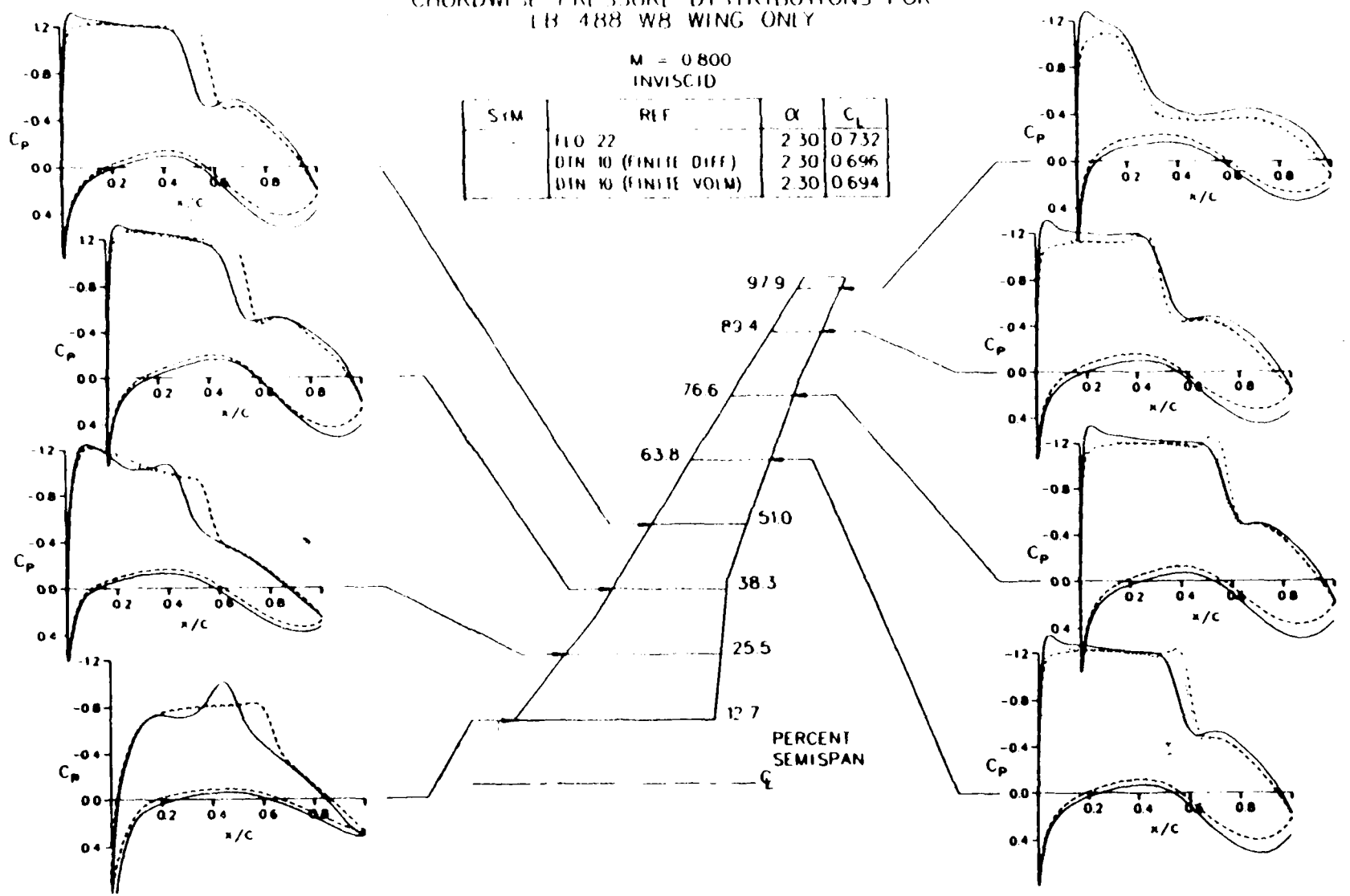

Figure 11. Comparison of finite-difference, finite volume and FLO-22 solutions for a Douglas LB-488 wing at $M_\infty = 0.8$ and $\alpha = 2.3°$.

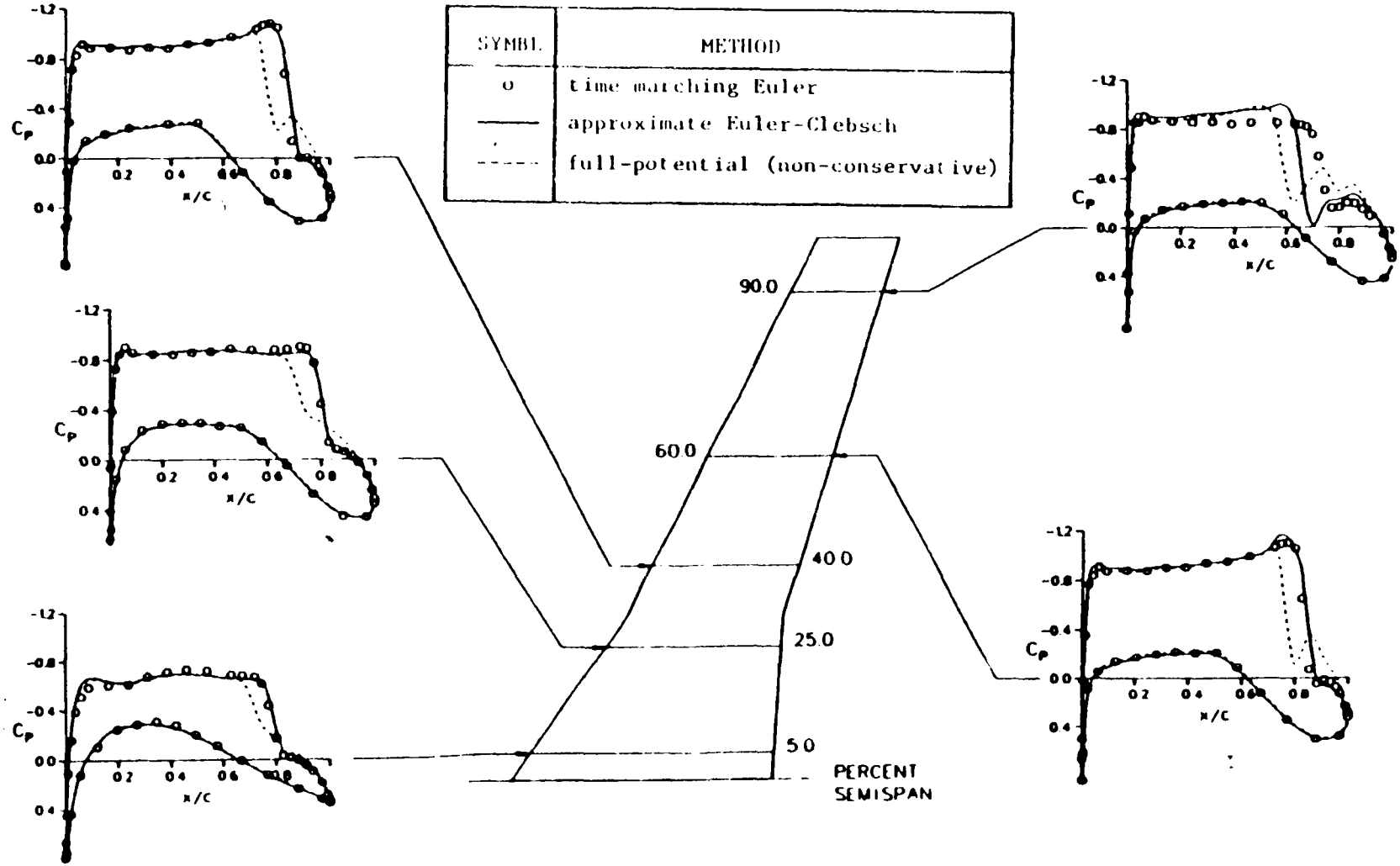

Figure 12. Comparison of Euler, Euler correction and partially conservative solutions for NASA swept wing at $M_\infty = 0.833$ and $\alpha = 1.75°$.

solution is in good agreement with the time-marching Euler solution, except near the wing-tip region. On the other hand, the nonconservative full-potential method tends to predict earlier shock formation and weaker shock strength compared to the time-marching Euler method. Moreover, the after-shock reexpansion phenomenon appears in the nonconservative full-potential solution when the shock becomes strong, for example, at the 40% and 60% span locations.

Near the wing-tip region, both the full-potential and the Euler-Clebsch methods predict a higher suction peak than the time-marching Euler method. Moreover, large after-shock reexpansions are found in the solutions of the two former methods. Figure 13 gives comparisons of sectional C_ℓ, C_d and C_m between the results obtained using these three methods. Finally, Figure 14 shows the convergence histories of average residuals and percent of supersonic points in the computational domain as a function of work unit by the full-potential and Euler-Clebsch methods. This figure clearly demonstrates that the Euler-Clebsch method has the same convergence rate as the full-potential method with about 20% more computational time per work unit. Moreover, the computer storage requirements in these two methods are approximately the same. On the other hand, the time-marching Euler method is estimated to require nearly one order of magnitude more computational time than the full-potential method.

At zero angle of attack, the ONERA-M6 wing is nonlifting and hence does not have a trailing vortex sheet. Inaccuracies associated with the approximate modeling of the trailing vortex sheet can therefore be isolated in this test case. Figure 15 illustrates a comparison of the pressure distributions obtained at three spanwise locations using the Euler-Clebsch method, the nonconservative full-potential method, and the Onera/Matra time-marching Euler method. The Onera/Matra solution presented in the AGARD report [1] was chosen for comparison since it lies between the other AGARD solutions and has tabulated pressure data. In general the Euler-Clebsch method predicts shock location and shock strength better than the full-potential method. The shock locations predicted by the Euler-Clebsch method are consistently slightly downstream of those predicted by the time-marching Euler solution, except near the wing-tip region. For example, at the 80% span station, the Euler-Clebsch solution predicts the shock location slightly upstream of that predicted by the time-marching Euler solution. In addition, the study also indicates that the Euler-Clebsch method predicts a suction level in front of the shock slightly

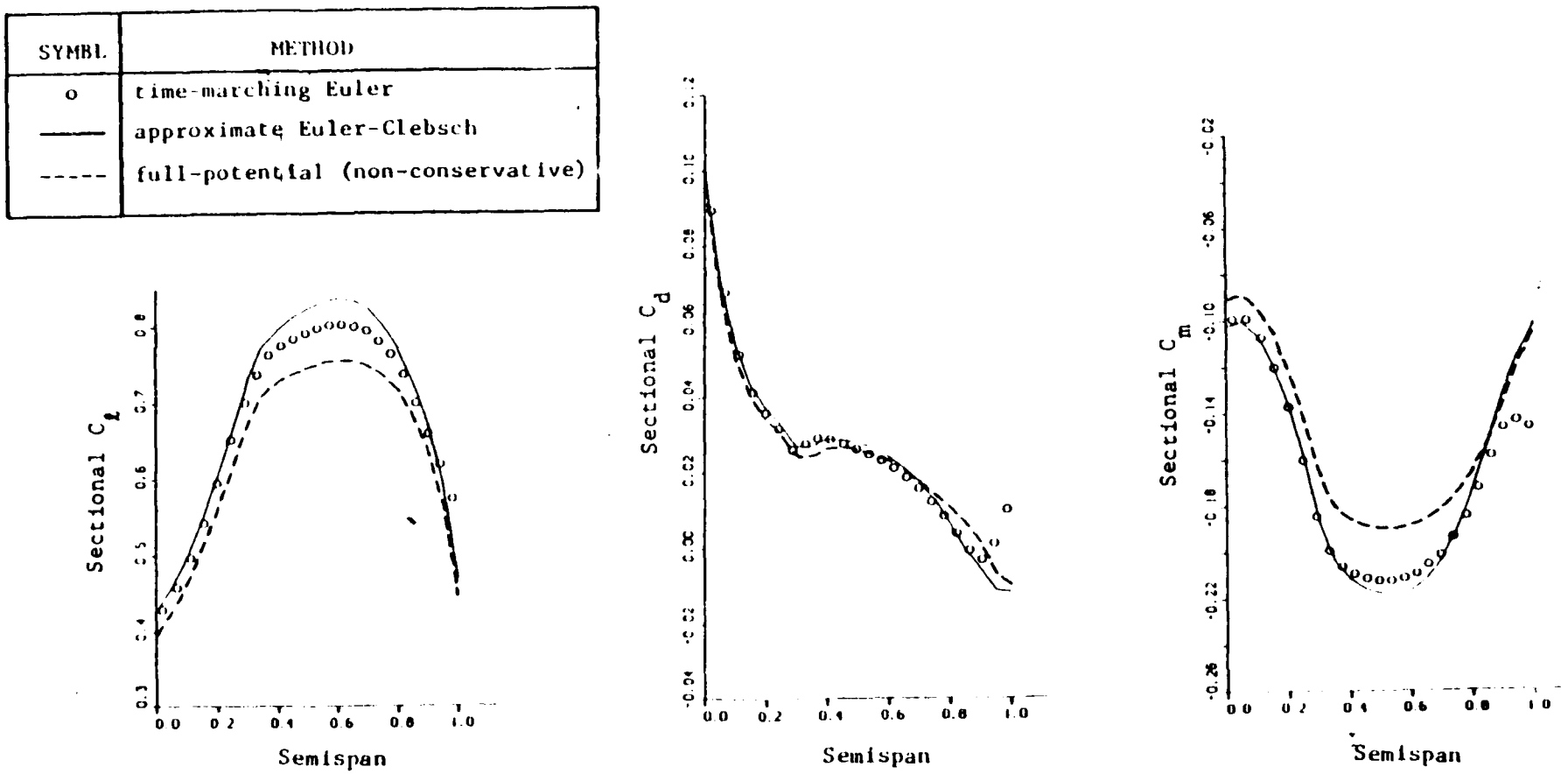

Figure 13. Comparison of computed sectional C_ℓ, C_d and C_m for NASA swept wing at M_∞ = 0.833 and α = 1.75°.

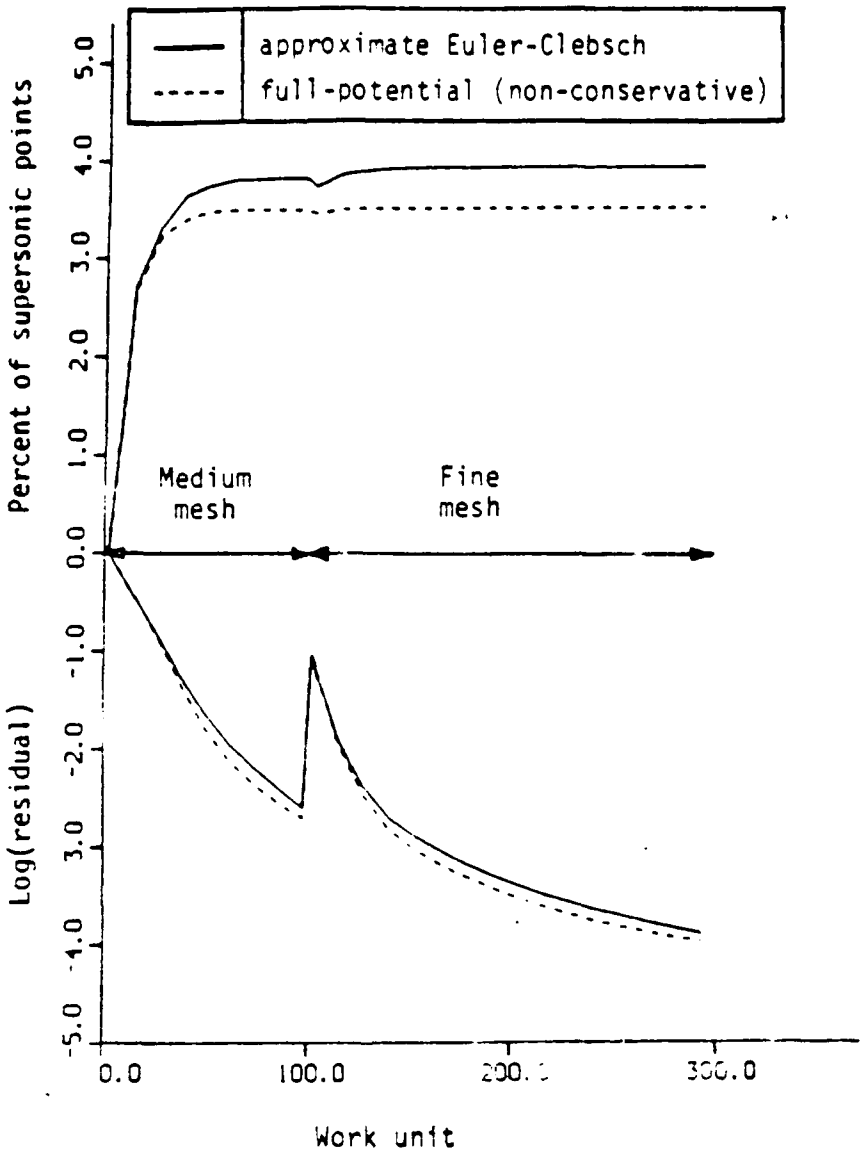

Figure 14. Comparison of convergence history for the solutions obtained for NASA swept wing at $M_\infty = 0.833$ and $\alpha = 1.75°$.

higher than that predicted by the time-marching Euler solution, hence the shock is stronger.

All of these discrepancies are very similar to those found in the NASA swept wing case, even though the trailing vortex sheet is absent in this example. Hence, it is believed that the disagreements around the wing-tip region in the results of these methods may be associated with the different ways in which the wing-tip boundary conditions are handled. However, due to the limited data available in the literature and the premature status of the time-marching Euler

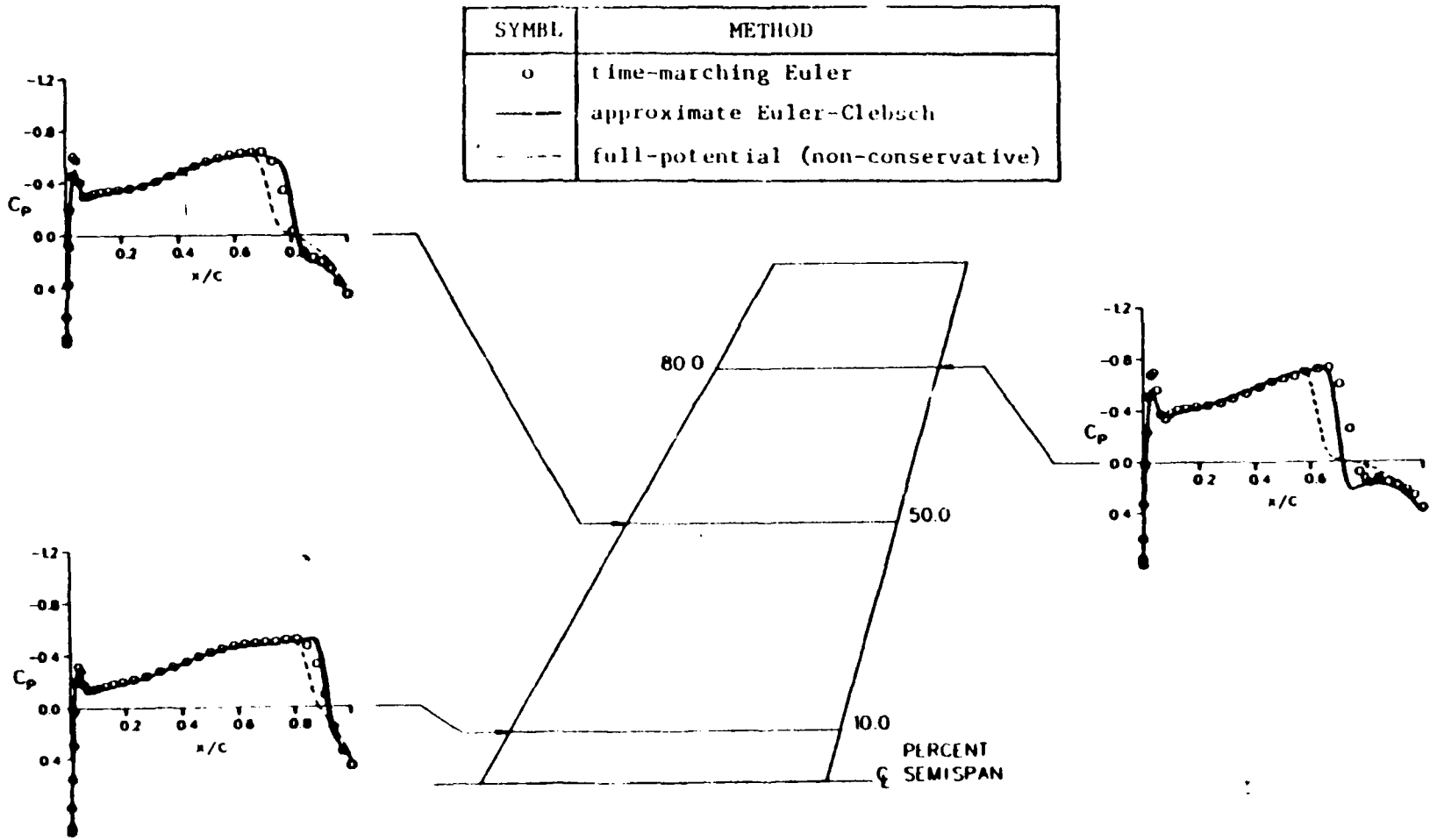

Figure 15. Comparison of computed pressure distributions for ONERA M6 wing at $M_\infty = 0.92$ and $\alpha = 0°$.

code at the present time, no definite conclusions can be drawn from these results as to the accuracy of the present method near the wing tip region.

6.4 Wing/Body Solutions

An example of a wing/body flowfield calculation is demonstrated for an F-14 model [33]. The input geometry is shown in Fig. 16. Near the wing root, there is a leading-edge break, where the leading-edge sweep angle changed from 68° to 22°. The inlet entrance is modeled by a flat surface where the no-flux condition is applied. The grid generation method of Chen, Vassberg and Peavey [28] is applied to generate a C-H-H grid, as shown in Figs. 17 and 18. Figure 17 shows a grid distribution on the wing and fuselage surfaces, while Fig. 18 shows a typical fuselage cross-sectional grid distribution at nearly midwing. The solutions obtained for wing-alone and wing/body cases are presented in Figs. 19 and 20 for M_∞ = 0.800 and α = 4°, and M_∞ = 0.900 and α = 2°, respectively, using the nonconservative scheme. The results show that the fuselage introduces a significant upwash effect on the pressure distribution on the wing surface. This effect is more pronounced near the wing root than near the wing tip. The slight oscillation in the wing/body solutions near the leading edge

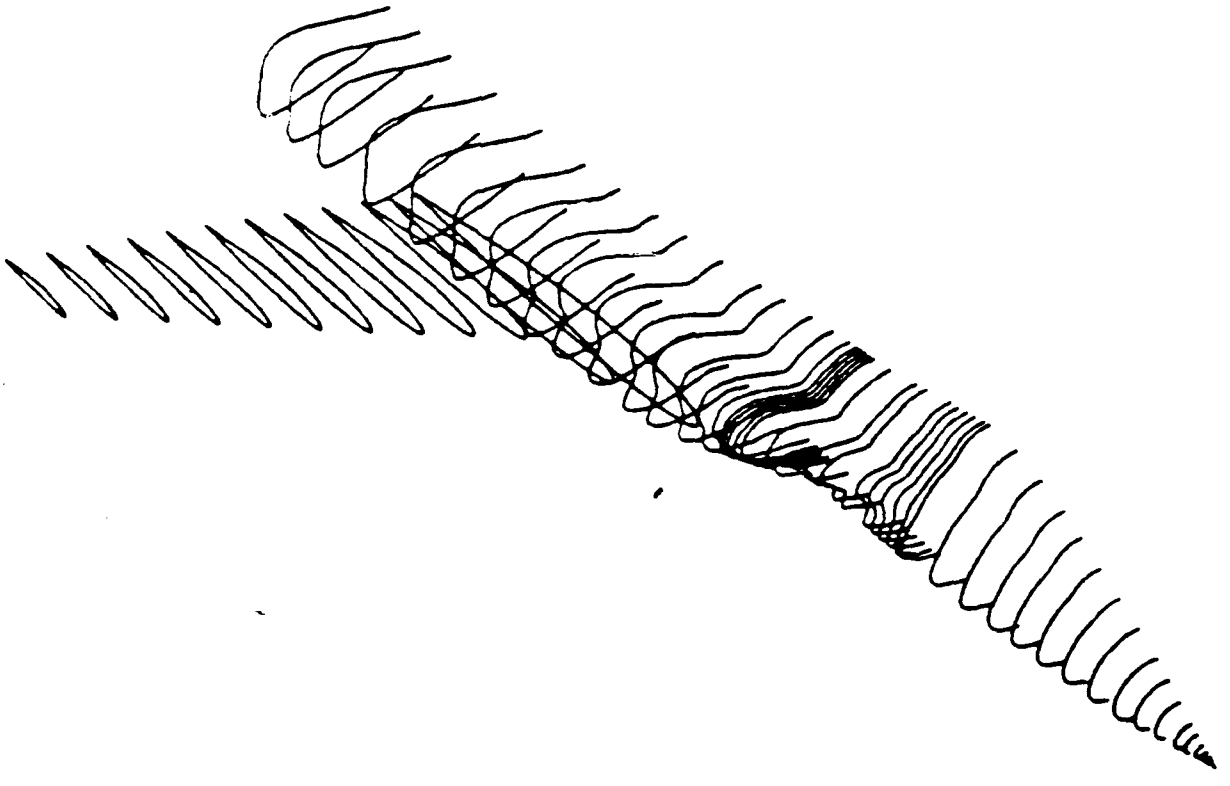

Figure 16. An input geometry for F-14 wing/body.

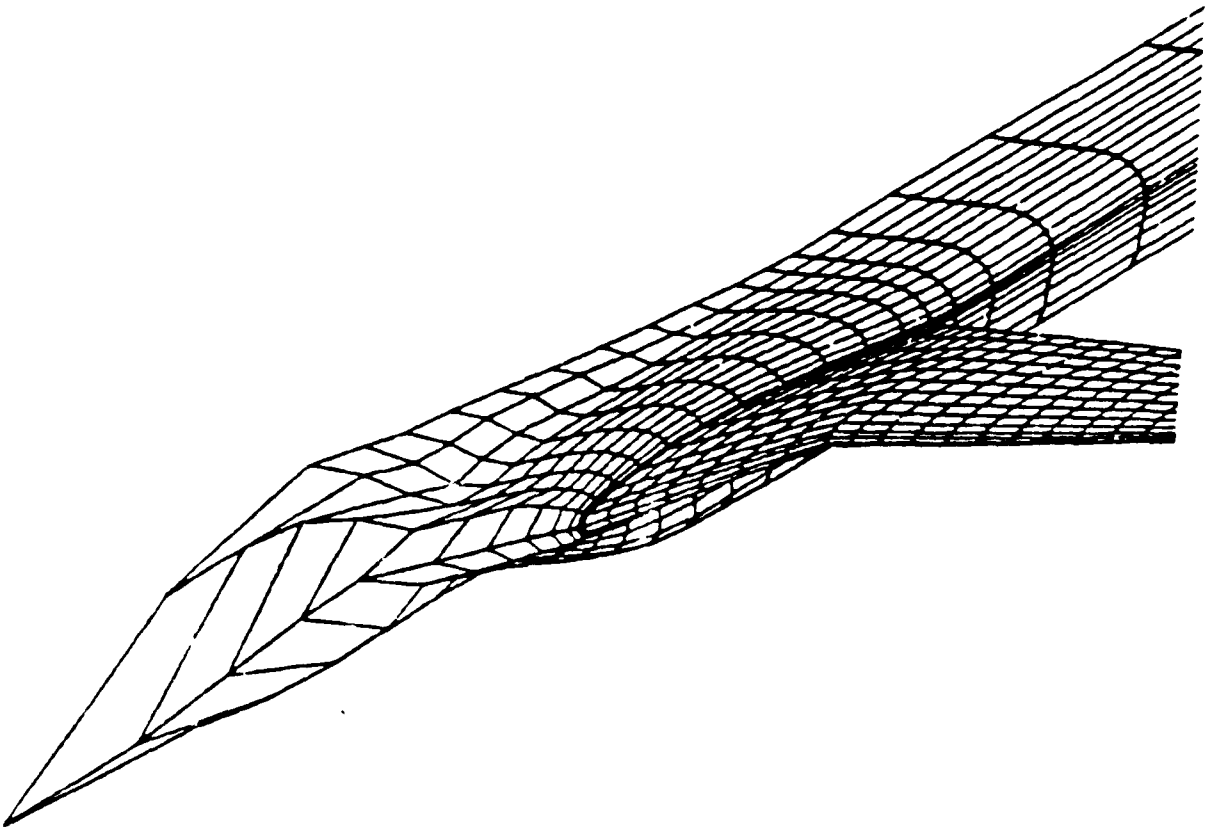

Figure 17. Surface grid distribution on the F-14 wing/body

is probably due to the mesh distortion caused by an unsmooth variation of the fuselage cross-sectional area.

Comparisons of solutions obtained for the F-14 wing/body using the fully conservative full-potential method and the present Euler-Clebsch method are presented in Figs. 21 and 22 for $M_\infty = 0.85$ and $\alpha = 4°$, and $M_\infty = 0.9$ and $\alpha = 2°$, respectively. Figure 21 shows that the fully-conservative full-potential solution predicts stronger and more downstream shocks than the Euler-Clebsch solution. An exceptionally high suction peak appears near 35% semispan location in the Euler-Clebsch solution; this may be due to the slope discontinuity at the leading-edge break. Figure 22 presents the solution at a higher Mach number, $M_\infty = 0.900$ and a lower angle of attack, $\alpha = 2°$. The Euler-Clebsch method predicts a shock very close to the trailing edge, while the fully-conservative full-potential method fails to give a converged solution. Figure 23 presents three solutions obtained for the F-14 wing/body using the Euler-Clebsch method at Mach numbers $M_\infty = 0.85$, 0.90 and 0.95, respectively, and at angle of attack

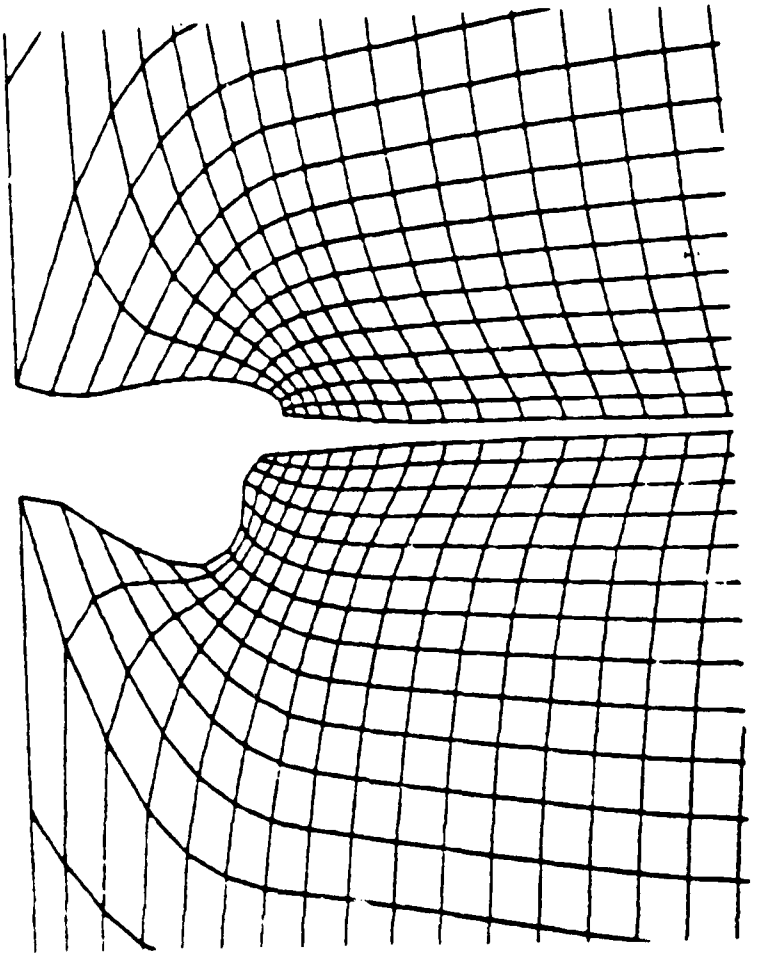

Figure 18. A cross-sectional grid distribution for the F-14 wing/body

$\alpha = 2°$. Strong shocks are predicted on the upper surface at all freestream Mach numbers, and a second shock is developed on the lower surface for the $M_\infty = 0.95$ case. Because of the appearance of the lower-surface shock and a significantly reduced pressure plateau on the upper surface, the total lift drops as the freestream Mach number increases from 0.900 to 0.950. The Kutta condition for the solution of $M_\infty = 0.95$ near the wing tip is not satisfied exactly due to the limitation of the approximate Euler-Clebsch assumptions. As explained in Section 5.4, the Kutta condition is satisfied under the assumption that the velocity jump across the wake, Δq, is much smaller than the freestream velocity. As the shock becomes stronger, the above assumption is no longer valid; therefore the pressures at the upper and lower trailing edges become further apart, as shown in the solutions of $M_\infty = 0.95$. Whether the Kutta condition

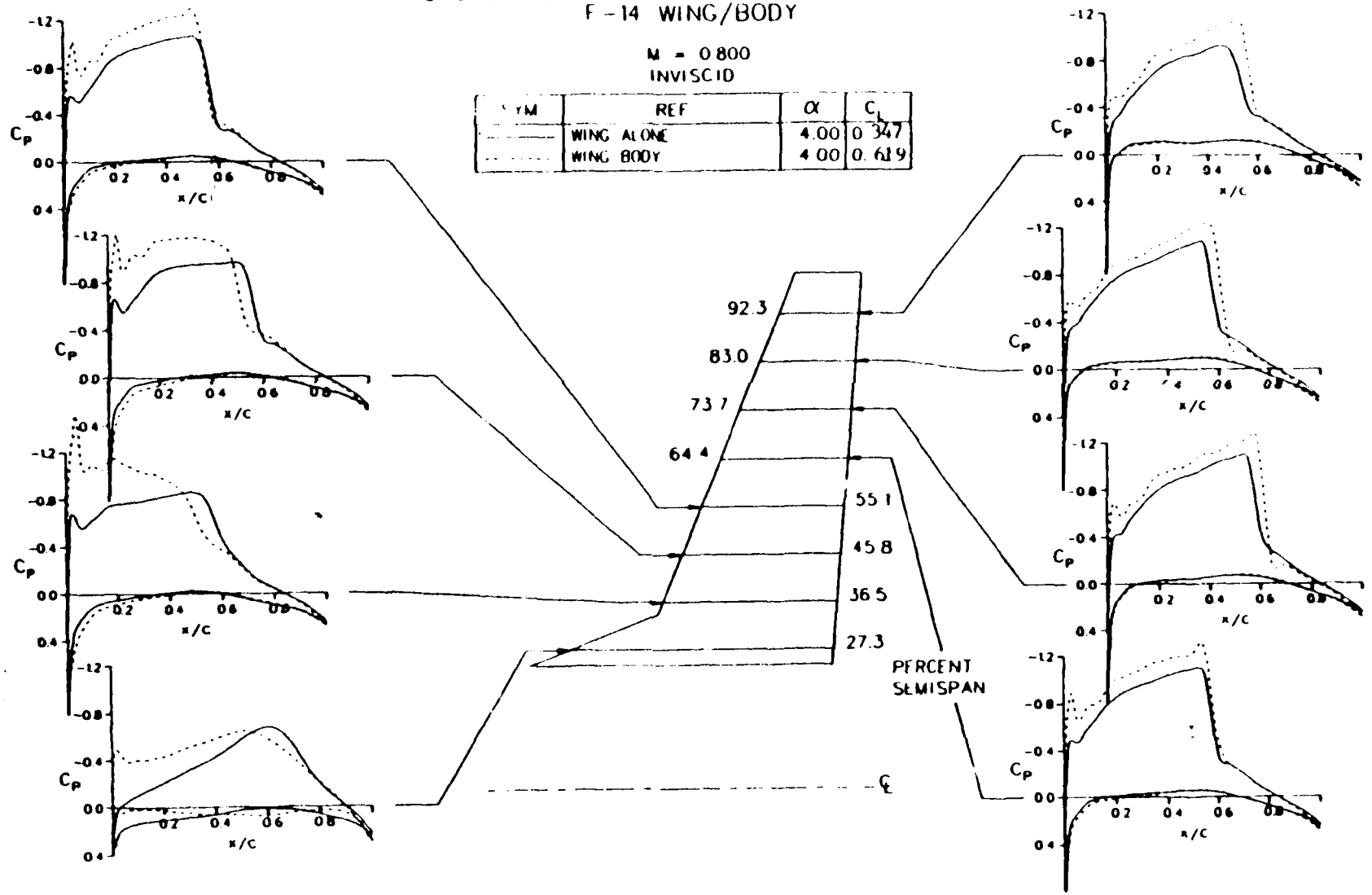

Figure 19. Comparison of F-14 wing alone and wing/body solutions at M_∞ = 0.800 and α = 4°.

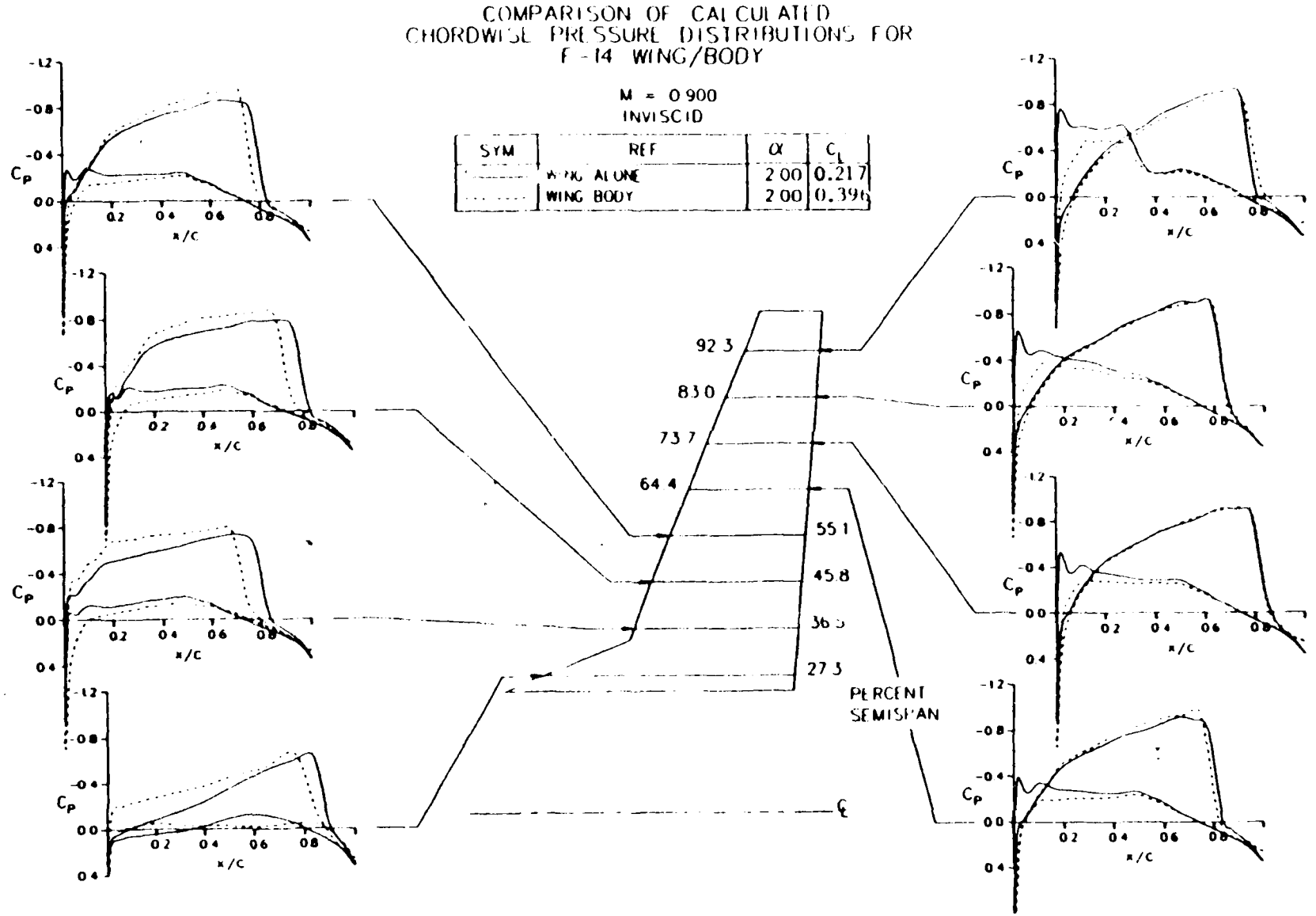

Figure 20. Comparison of F-14 wing alone and wing/body solutions at $M_\infty = 0.900$ and $\alpha = 2°$.

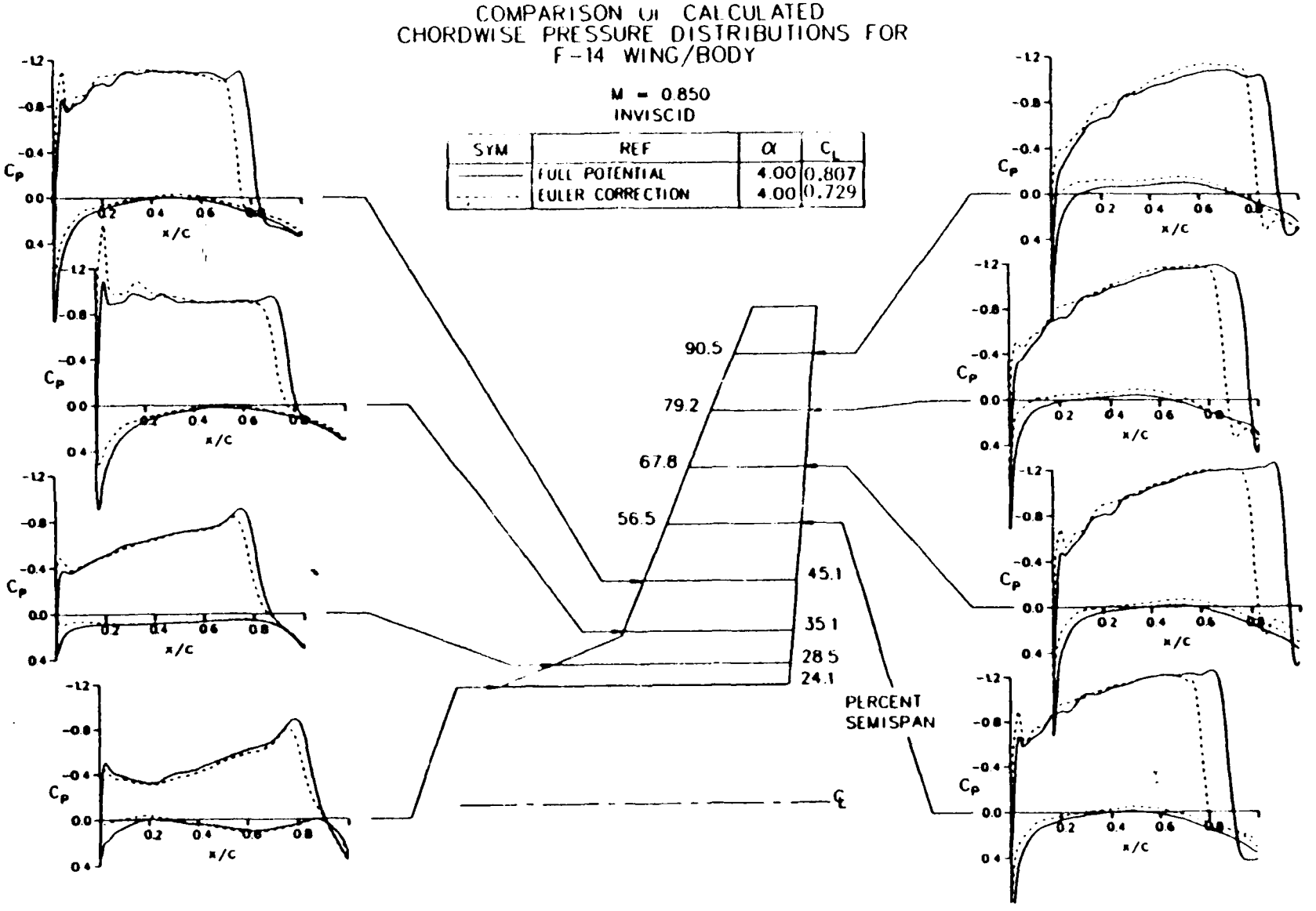

Figure 21. Comparison of the full-potential and Euler-Clebsch solutions for the F-14 wing/body at M_∞ = 0.85 and α = 4°.

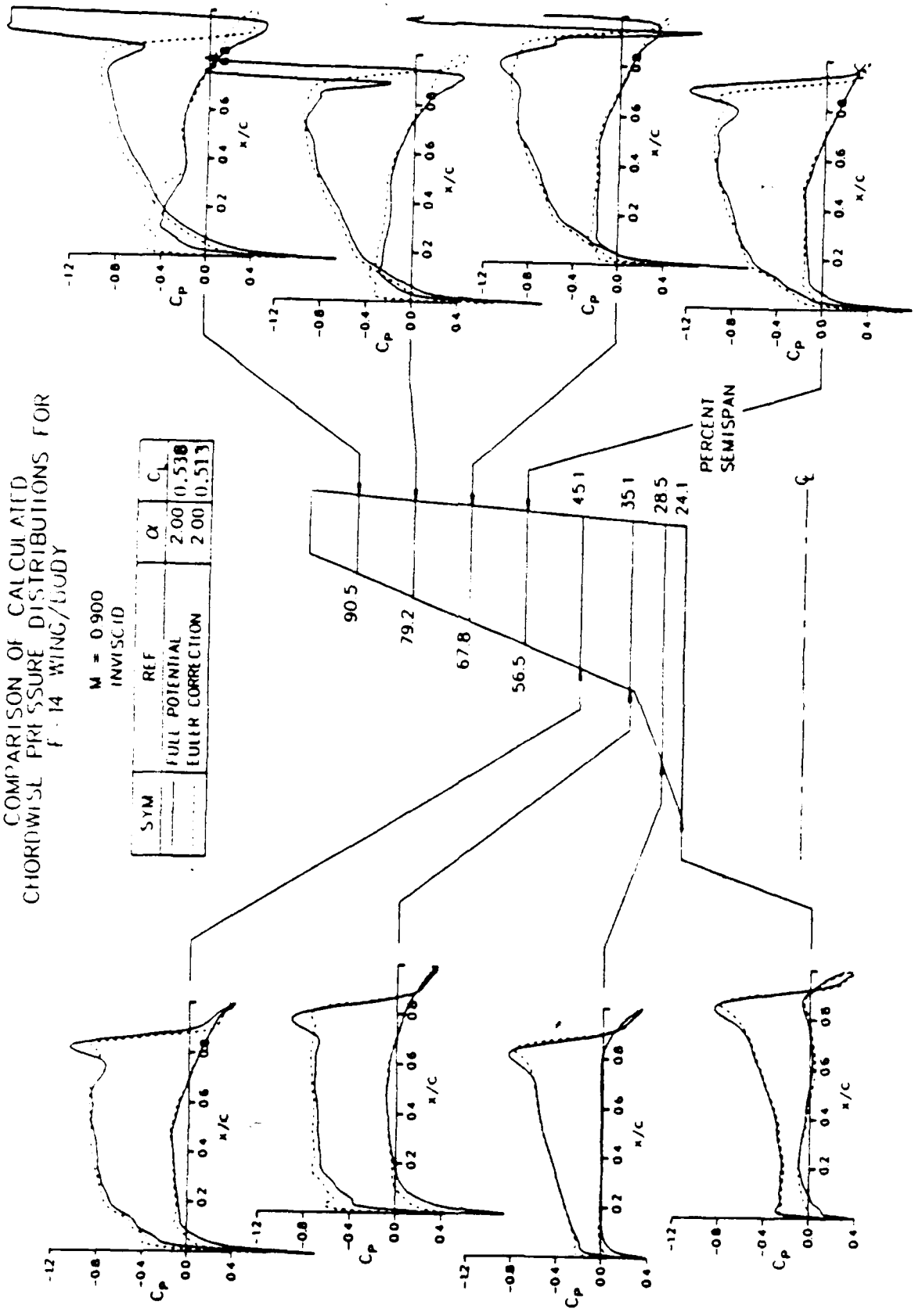

Figure 22. Comparison of the full-potential and Euler-Clebsch solutions for the F-14 wing/body at M_∞ = 0.900 and α = 2°.

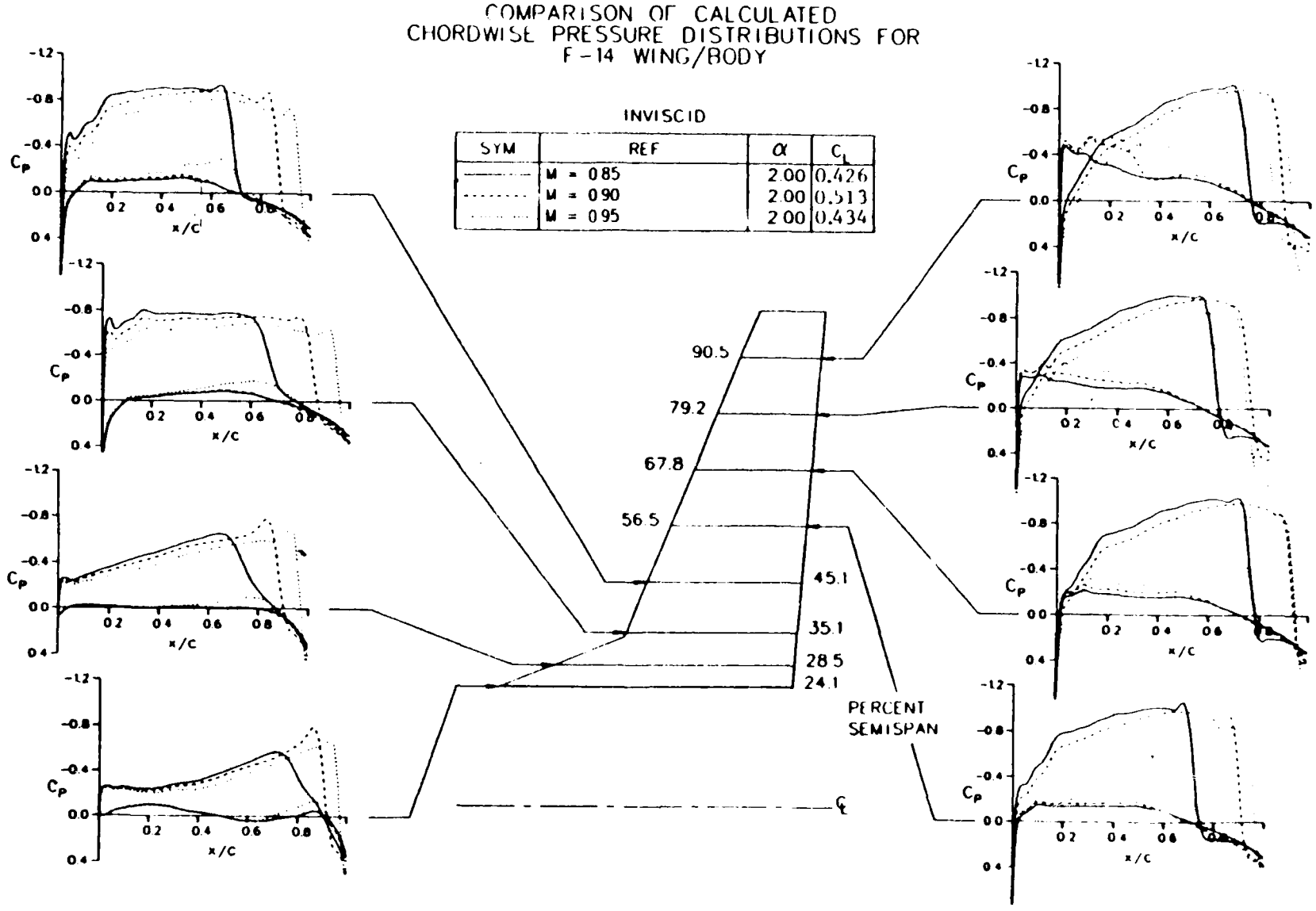

Figure 23. Comparison of the Euler-Clebsch solutions obtained for the F-14 wing/body at M_∞ = 0.85, 0.90 and 0.95 and α = 2°.

can be better satisfied by using the exact Euler-Clebsch method in the three-dimensional case should be further investigated.

The F-14 wing/body solutions presented in Figs. 19 through 23 are obtained for a wing with a leading-edge break, located at about 34% semispan location, where the leading-edge sweep angle changes from 67° to 22°. The total lift coefficients computed for this configuration at $M_\infty = 0.8$ and $\alpha = -4.3°$, $-2.65°$, $-1°$, $0°$, $1°$, $2°$, $3.05°$ and $4.05°$ are presented in Table 1 and Fig. 24 and compared with the test data of Bavitz [34]. In the calculations, the fuselage is extended to downstream infinity with constant cross-section, as shown in Fig. 17, the tail section is not modeled, and the surface pressure integration for the total lift is performed on the entire wing and part of the fuselage from the nose to about one root chord length downstream of the wing trailing edge. The reference wing area is chosen to be the extended wing planform area which is computed by linearly extending the 22° leading-edge line and the trailing-edge line from the leading-edge break to the vertical symmetry plane. The computed total lift coefficients agree fairly well with the test data, as shown in Fig. 24, despite the tail section and the viscous effect not being included in the calculation.

Table 1. Comparison of experimental and computed total lift coefficients for the F-14 wing/body configuration at $M_\infty = 0.800$

Data Points	a	$C_L)_{exp}$	$C_L)_{calc}$
1	-4.3°	-0.410	-0.3685
2	-2.65°	-0.185	-0.1755
3	-1°	0.020	0.0206
4	0°	0.150	0.1412
5	1°	0.280	0.2631
6	2°	0.410	0.3863
7	3.05°	0.515	0.5183
8	4.05°	0.625	0.6390

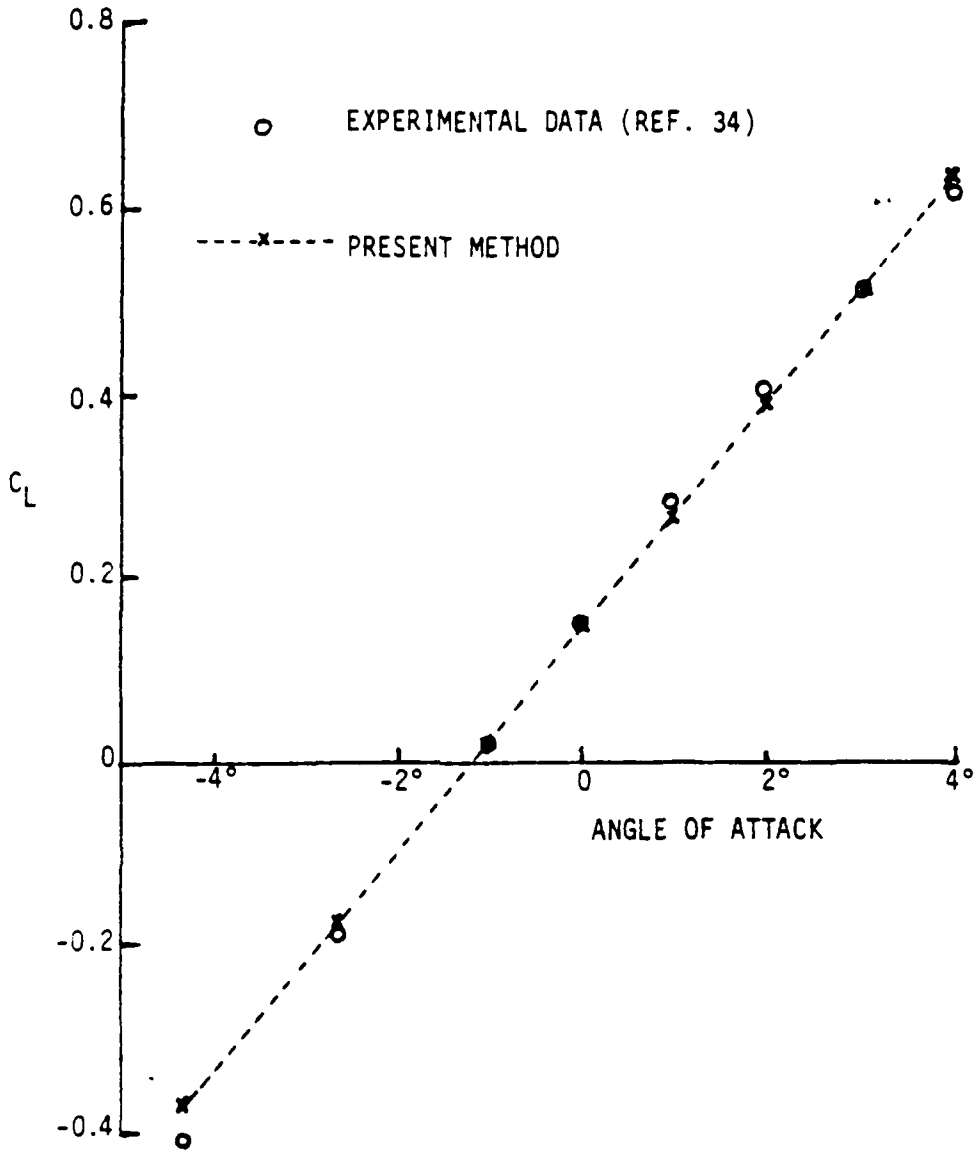

Figure 24. Comparison of computed lift coefficients with test data for the F-14 wing/body at $M_\infty = 0.800$.

7.0 CONCLUDING REMARKS

The full-potential and time-marching Euler methods are two of the most promising transonic computational methods at the present time. Each method has its own advantages over the other and, therefore, has its own special applications. The work reported has demonstrated that the full-potential method for transonic flowfield calculations can be further improved by including the rotational effect, introduced due to entropy jump across the shocks, as in the present two- and three-dimensional Euler correction methods based on the Clebsch transformation. The approximate Euler-Clebsch method has been developed for both two- and three-dimensional flows, while the exact Euler-Clebsch method is implemented only for the two-dimensional case. The results for transonic airfoil flows show that the approximate and the exact Euler-Clebsch solutions generally agree well. The total pressure loss across the shocks is included in the present method in conjunction with the use of the Rankine-Hugoniot relation, while this is neglected in the conventional full-potential methods. The convection of the vorticity is computed along streamlines in the exact Euler-Clebsch method and along the mesh lines in the approximate Euler-Clebsch method, while the vorticity is dissipated in the time-marching Euler method because of the need to add artificial dissipation terms. The implementation of the present method is straightforward. The present scheme based on the Clebsch transformation can be applied in most of the existing full-potential methods, not only for calculating more accurate shocks, but also for modeling two- and three-dimensional rotational flows such as flows downstream of actuator disks [35,36].

A study of finite-volume and finite-difference formulations of the full-potential equation is presented. The solutions obtained by using both formulations agree well; the finite volume method calculates the density term implicitly while the finite-difference method does not. The present method computes transonic flows more accurately than the full-potential methods and gives solutions agreeing better with the time-marching Euler solutions. However, for flows with very strong shocks, the present approximate Euler-Clebsch method does not exactly satisfy the Kutta condition. Further work to improve the two-dimensional exact Euler-Clebsch method and to extend it to three dimensions is recommended.

8.0 ACKNOWLEDGMENT

The authors wish to express their gratitude to T.C. Tai of the David Taylor Research Center for his interest and fruitful discussions during the course of this study, and to Greg Huson of the David Taylor Research Center for his assistance in providing the F-14 geometry and experimental data and also for his careful review of this report.

9.0 REFERENCES

1. Test Cases for Inviscid Flow Field Methods, AGARD-AR-211, 1985.

2. Margason, R.J.: Review and Evaluation of Euler Methods Test Case Results. AIAA Euler Solvers Workshop, Monterey, CA, Aug. 1987.

3. Chen, L.T.: Higher-Order Computational Methods for Transonic Wing/Body Flowfields. Final Contract Rept., DTNSRDC-ASED-CR-03-82, Sept. 1982.

4. Chen, L.T.: A More Accurate Transonic Computational Method for Wing-Body Configurations. AIAA J., Vol. 21, pp. 848-855, June 1983.

5. Jameson, A. and Caughey, D.A.: A Finite-Volume Method for Transonic Potential Flow Calculation. Proceedings of AIAA 3rd Computational Fluid Dynamics Conf., Albuquerque, NM, pp. 35-54, June 1977.

6. Hafez, M., Lovell, D.: Entropy and Vorticity Corrections for Transonic Flows. AIAA Paper 83-1926, 1983.

7. Klopfer, G.H. and Nixon, D.: Nonisentropic Potential Formulation for Transonic Flows. AIAA Paper No. 83-0375, 1983.

8. Lock, R.C.: A Modification to the Method of Garabedian and Korn. In Notes on Numerical Fluid Mechanics, Numerical Methods for the Computation of Inviscid Transonic Flows with Shock Waves. (eds. A. Rizzi and H. Viviand), Vol. 3, Friedr. Vieweg & Sohn, Braunschweig/Wiesbaden, 1979.

9. Chen, L.T.: A Modified Shock-Point Operator with Stagnation-Density Correction. In Numerical and Physical Aspects of Aerodynamic Flows II (ed. T. Cebeci), Springer-Verlag, New York, pp. 351-365, 1984.

10. Chen, L.T., Clark, R.W. and Vassberg, J.C.: Improvements in Transonic Airfoil Potential Flow Calculations. AIAA Paper 85-1642, 1985.

11. Brown, E.F., Brecht, T.J.F. and Walsh, K.E.: A Relaxation Solution of Transonic Nozzle Flows Including Rotational Flow Effects. J. of Aircraft, Vol. 14, pp. 944-951, Oct. 1977.

12. Sokhey, J.S.: Transonic Flow Around Axisymmetric Inlets Including Rotational Flow Effects. AIAA Paper 80,341, 1980.

13. Ecer, A., Akay, H.U.: A Finite Element Formulation of Euler Equations for the Solution of Steady Transonic Flows. AIAA J., Vol. 21, pp. 343-350, 1983.

14. Ecer, A.: Block Sturctured Solution of Three-Dimensional Euler Equation Using the Finite-Element Method. AIAA Ppaer 87-0351, Jan. 1987.

15. Tai, T.C.: Hybrid Approach to Transonic Inviscid Flow with Moderate to Strong Shock Wave. Transonic Aerodynamics (ed. D. Nixon) Vol. 21, Progress in Astronautics and Aeronautics, 1982.

16. Dang, T.Q. and Chen, L.T.: An Euler Correction Method for Two- and Three-Dimensional Transonic Flows. AIAA Ppaer 87-522, Jan. 1987.

17. Chen, L.T.: Improved Finite-Difference Scheme for Transonic Airfoil Flowfield Calculations. AIAA J., Vol. 20, p. 218, 1982.

18. Murman, E.M. and Cole, J.D.: Calculation of Plane Steady Transonic Flows. AIAA J., Vol. 9, pp. 114-121, June 1971.

19. Hawthorne, W.R.: On the Theory of Shear Flow. MIT GTL Rept. No. 88, 1966.

20. Dang, T.Q.: A Three-Dimensional Blade Design Method to Control Secondary Flow. Ph.D. Thesis, Dept. of Aero/Astro, MIT, Cambridge, June 1985.

21. McCune, J.E. and Hawthorne, W.R.: The Effects of Trailing Vorticity on the Flow Through Highly-Loaded Cascades. J. Fluid Mech., Vol. 74, pp. 721-740, 1976.

22. Chen, L.T. and McCune, J.E.: Comparison of 3-D Quasi-Linear Large Swirl Theory with Measured Outflow from a High Work Compressor Rotor. MIT GTL Rept. No. 128, 1975.

23. Tan, C.S.: Vorticity Modeling of Blade Wakes Behind Isolated Annular Blade Rows: Induced Disturbances in Swirling Flows. ASME J. of Eng. for Power, Vol. 103, No. 2, Apr. 1981.

24. Hawthorne, W.R., McCune, J.E., Mitchell, N.A. and Tan, C.S.: Nonaxisymmetric Flow Through an Annular Actuator Disk: Inlet Distortion Problem. ASME J. of Eng. for Power, Vol. 100, 1978.

25. Jameson, A.: Acceleration of Transonic Potential Flow Calculations on Arbitrary Meshes by the Multiple Grid Method. AIAA Paper No. 79-1458, July 1979.

26. Shmilovich, A. and Caughey, D.A.: Application of the Multi-Grid Method to Calculations of Transonic Potential Flow About Wing-Fuselage Combinations. NASA SP-2202, pp. 101-130, Oct. 1981.

27. Caughey, D.A.: Multi-Grid Calculation of Three-Dimensional Transonic Potential Flows. AIAA Paper No. 83-374, Jan. 1983.

28. Chen, L.T., Vassberg, J.C. and Peavey, C.C.: A Transonic Wing-Body Flowfield Calculation with Improved Grid Topology and Shock-Point Operators. AIAA J., Vol. 12, pp. 1877-1884, Dec. 1985.

29. Potter, D.: Computational Physics. John Wiley & Sons, 1973.

30. Jameson, A., Schmidt, W. and Turkel, E.: Numerical Solutions of the Euler Equations by Finite-Volume Methods Using Runge-Kutta Time-Stepping Schemes. AIAA Paper 81-1259, June 1981.

31. Chen, L.T., Li, S. and Chen, H.: Calculation of Transonic Airfoil Flows by Interaction of Euler and Boundary-Layer Equations. AIAA Paper 87-521, 1987.

32. Henne, P.A. and Hicks, R.M.: Wing Analysis Using a Transonic Potential Flow Computational Method. NASA TM-78464, July 1978.

33. McBride, A.: Supersonic Wind Tunnel Tests of 1/22 Scale Model of the Grumman Design 303-E Aircraft in the Convair High Speed Wind Tunnel Series II. Vol. I, Grumman Rept. AER/T-CONVAIR-2, Aug. 1969.

34. Bavitz, P.C.: F-14A Transonic Aerodynamic Envelope, (U)... Grumman Aircraft Engineering Corp. Report GAEC-A-51-335-R-70-2 (or NASA Report AD-510-894), Feb. 1970.

35. Dang, T.Q.: Simulation of Propeller Effects Using An Actuator Disk and the Euler-Clebsch Method. McDonnell Douglas Report MDC J4953 (in preparation).

36. Chen, L.T., Yu, K.C. and Dang, T.Q.: A Transonic Computational Method for Calculating Flowfields About an Aft-Fuselage Mounted Nacelle/Pylon Configuration With/Without Propeller Power Effect. McDonnell Douglas Report MDC-J4947 (in preparation).

END

DATE

FILMED

6-88

DTIC